1

2 DR. AKASH KOPPA (Orcid ID : 0000-0001-5671-0878)

3 DR. THOMAS HOPSON (Orcid ID : 0000-0002-4595-7274)

4

5

7

8

9 **A Scalable Earth Observations-Based Decision Support System for Hydropower Planning**

10 **in Africa**

11 Akash Koppa, Mekonnen Gebremichael, Thomas M. Hopson, Emily Riddle, Jennifer Boehnert, Daniel P.

12 Broman

13 Department of Civil and Environmental Engineering (Koppa, Gebremichael), University of California, Los

14 Angeles, California, USA (Correspondence to Koppa: akashkoppa@ucla.edu)

15 Hydro-Climate Extremes Lab (H-CEL) (Koppa), Faculty of Bioscience Engineering, Ghent University,

16 Coupure Links 653, 9000 Ghent, BelgiumResearch Applications Laboratory (Hopson, Riddle, Boehnert),

17 National Center for Atmospheric Research, Boulder, CO, USA

18 Department of Civil, Environmental, and Architectural Engineering (Broman), University of Colorado

19 Boulder, Colorado, USA

20 Water and Environmental Resources Division (Broman), United States Bureau of Reclamation, Colorado,

21 USA

22 **Research Impact Statement:** A novel decision support system based on earth observation

23 satellites, ensemble climate forecasts and hydrologic models for hydropower planning under deep

24 data uncertainty in Africa.

25 **ABSTRACT:** Hydropower is a key part of the increasing shift in power production from non-
26 renewables to renewable energy. In regions such as Africa, hydropower reservoirs are vital for
27 achieving several sustainable development goals, including clean water, energy, and poverty
28 elimination. However, the operations of hydropower reservoirs are often sub-optimal due to lack
29 of hydrologic data for generating reliable inflow forecasts. Here, we present a decision support
30 system (DSS) framework for hydropower planning at daily to seasonal timescales by combining
31 data from earth observation satellites (EOS) with ensemble climate forecasts from dynamical
32 models and hydrologic modeling. The large uncertainty inherent in satellite-based datasets is
33 overcome by using a data validation framework which does not require ground-based
34 measurements. In addition, an EOS evapotranspiration product is used as a proxy for streamflow
35 in calibrating hydrologic models. Compared to a DSS forced with a climatological forecast (zero-
36 skill), the hydropower production with the new DSS increased by 20%. The study highlights the
37 advantage of using data from EOS in overcoming the issue of data scarcity in water resources
38 applications, particularly in developing regions of the world such as Africa.

39 (**KEYWORDS:** hydropower; decision support system; remote sensing; water resources)

40   INTRODUCTION

41 Access to water and energy are essential for the development of the socio-economically vulnerable
42 regions of the world. In fact, clean water and energy constitute two (SDG6 and SDG7) out of the
43 seventeen sustainable development goals (SDGs) identified by the United Nations (Griggs *et al.*,
44 2013; Sachs, 2012) (https://sustainabledevelopment.un.org/). Effective water and energy resources
45 planning is necessary for not only achieving SDG6 and SDG7 but also plays an important role in
46 addressing other SDGs such as poverty elimination (SDG1), zero hunger (SDG2), and promotion
47 of sustainable cities and communities (SDG11). In this regard, hydropower, which lies at the nexus
48 of water and energy, has an important role to play. This is especially true in Africa, which has
49 witnessed significant growth in the construction of reservoirs, including those specifically
50 targeting hydropower production. With such an exponential increase in hydropower capacity, it is
51 crucial to operate these reservoirs in such a way that guarantees energy production is maximized,
52 not an easy task given the seasonal and annual variability of water availability under present
53 (Broman *et al.*, 2020) and future (Fletcher *et al.*, 2019) climatic conditions. The lack of optimal
54 reservoir operation causes more frequent power outages and associated economic losses, and

55 incurs substantial opportunity cost (Conway *et al.*, 2017; Sridharan *et al.*, 2019). These reasons

56 necessitate the development and implementation of decision support systems (DSSs) which can

57 provide reliable and effective information to decision makers, at the relevant time scales.

58 DSSs are used for the optimal operations of reservoirs for a variety of purposes. Typically, the

59 near-term (daily), sub-seasonal (weekly), and seasonal (monthly) releases from a reservoir serve

60 multiple purposes, such as domestic, industrial, and agricultural water supply, flood control,

61 hydropower, and the maintenance of environmental flows (Alemu *et al.*, 2011; Koppa,

62 Gebremichael, Zambon, *et al.*, 2019; Westphal *et al.*, 2003). A DSS consists of three parts: 1) an

63 inflow forecasting system which uses statistical or dynamical methods to generate possible

64 realizations of future inflow into the reservoir at the required timescales, 2) an optimization system

65 which employs either deterministic or stochastic programming techniques, based on the nature of

66 the inflow forecasts, to optimize reservoir outflows, and 3) a visualization support system interface

67 that communicates this information to the user in an effective way to meet their decision-making

68 process in a timely fashion. In the rest of the Introduction, we provide a brief overview of the three

69 enumerated DSS components and summarize the objectives of this study.

70 *Inflow Forecasting System*

71 The effectiveness of a DSS for hydropower planning is significantly influenced by the reliability

72 of the inflow forecasting system. Inflow forecasting systems generally fall into one of the

73 following two categories: (1) statistical modeling based on past streamflow observations, and (2)

74 dynamically driven hydrologic modeling forced by climate forecasts.

75 In the first category, statistical modeling techniques such as autoregressive moving average and

76 neural networks which sample from past observation of inflows, are used to generate the forecasts

77 (Cuo *et al.*, 2011; Li *et al.*, 2017). Several factors hinder the application of such an inflow

78 forecasting system in Africa, of which in-situ data scarcity and inaccessibility are the most

79 significant, because the lack of reliable long-term inflow information adversely impacts the

80 accuracy of statistical models of forecasting.

81 In the second category, dynamic forecasts of reservoir inflows are generated with computational

82 physics-based climate and hydrologic models. The emergence of ensemble climate and hydrologic

83 forecasting in the last decade has shown potential for improving the quality of the forecasts, and

84 hence forecast-informed decision making (Alfieri *et al.*, 2013; Benninga *et al.*, 2017). While this

85 category has shown value in generating dynamic forecasts and acknowledging some uncertainties

86 in the forecasts, it is limited by the large range in ensemble members and questions about which

87 ensemble forecast products are reliable. In addition, reliable calibration of spatially distributed

88 hydrologic models for forecasting purposes are largely dependent on the availability of streamflow

89 measurements.

90 In our opinion, the next advancement in the inflow forecasting system in regions with reduced *in*

91 *situ* monitoring would be to develop a methodology that accurately quantifies the uncertainty in

92 the climate ensemble forecast products and reduces the uncertainty to a level that is useful for

93 decision making. Therefore, in this study, we propose a new approach for inflow forecasting

94 system that is particularly appropriate in data-scarce regions, such as Africa. This approach is to

95 utilize Earth Observing System (EOS) data to both dynamically adjust the climate forecasts

96 provided by climate forecast centers, while also utilizing the EOS data with novel techniques to

97 calibrate the hydrologic models of watersheds with limited surface measurements.

98 The value of EOS in enabling improved water resources management in data scarce regions is well

99 recognized (Sheffield *et al.*, 2018). The development of improved EOS over the last fifty years has

100 resulted in vast amounts of direct and indirect observations of nearly all the water and energy

101 balance components required for modeling the earth's terrestrial processes, including its hydrology

102 (Lettenmaier *et al.*, 2015). Although, EOS data have been extensively used in climate and

103 hydrological modeling and forecasting through data assimilation (Crow and Ryu, 2009; Mazrooei

104 and Sankarasubramanian, 2019) and model calibration (Koppa, Gebremichael, and Yeh, 2019;

105 López *et al.*, 2017; Rakovec *et al.*, 2016; Zink *et al.*, 2018) or directly as forcing inputs, the utility

106 of such data for water and energy resources planning, in general, and hydropower reservoir

107 operation, specifically, has not been sufficiently explored.

108 One of the key challenges in utilizing EOS data products is to choose which data products to use.

109 There are many EOS data products for the same variable (e.g., precipitation) with large differences

110 amongst them owing to differences in satellites, sensors and retrieval algorithms. In addition, the

111 choice of EOS data products may have to take into account their joint performance to ensure some

112 realism, for example, the closure of energy and water balance. This is corroborated by several

113 findings (Bitew *et al.*, 2012; Koppa, Gebremichael, and Yeh, 2019) who showed that the use of

114 EOS data products for only one variable may show good performance in simulating the streamflow

115 at the outlet of the catchment, but it may have large errors and unrealistic performance in

116 simulating other water balance components, indicating that such an approach may not work in

117 simulating even streamflow in the case of cascading hydropower reservoirs. Therefore, new

118 methodologies need to be developed that advance the use of EOS data for hydropower reservoir

119 planning, particularly in Africa where ground validation data are lacking.

120 *Optimization System*

121 The optimization of a cascade of hydropower dams, using an ensemble of streamflow forecasts, is

122 generally carried out using stochastic programming with recourse models (Yeh, 1985). In such

123 models, the system of reservoirs is optimized for the entire forecast horizon but the release

124 decisions for only the first-time step (referred to as 'first stage') is adopted. Then, the forecast

125 horizon is moved forward by one stage and the optimization procedure is repeated. Although the

126 value of stochastic inflow forecasts in hydropower optimization is well studied (Séguin *et al.*,

127 2017), an assumption inherent in such optimization models is that the first stage (day, week,

128 month) forecast is deterministic. In other words, the forecast for the first stage is assumed to be

129 sufficiently accurate such that a single deterministic forecast for the first stage is deemed enough

130 for the optimization of reservoirs. When new information regarding the inflow into reservoirs are

131 available, the whole system is validated, and the required adjustments are made to the DSS before

132 the start of the next stage. Several studies employ this approach for the operation of reservoir

133 cascades (Etkin *et al.*, 2015; Wang *et al.*, 2012). However, such an approach is dependent on the

134 availability of reservoir inflows at regular intervals for the validation of the entire DSS, which may

135 not be possible in data scarce regions such as Africa. Here, we implement a new stochastic

136 programming with recourse model which considers the first stage to be also stochastic (Koppa,

137 Gebremichael, Zambon, *et al.*, 2019). In addition, we implement the conventional stochastic

138 programming with recourse model and a purely deterministic optimization model to enable

139 decision making under data scarcity and uncertainty.

140 *Visualization Support System*

141 The effectiveness of a DSS for hydropower planning is significantly enhanced by providing a

142 coherent interface between the technical outputs of the inflow forecasting and optimization

143 systems that then communicates this information to the user in an effective way to meet their

144   decision-making process, all in a timely fashion. The scale of the information produced by

145   hydrometeorological services and climatological centers can often be overwhelming to a user. As

146   an example, ensemble rainfall forecasts at a single location from a single weather center can easily

147   comprise over 3000 data points for a forecast going out to two weeks in advance – a well-designed

148   visualization and support system then should consolidate and filter such information using expert

149   knowledge of the data's relevance to the unique decision making process of the user. A number of

150   systems have been developed that have been shown to be effective in communicating timely,

151   coherent, relevant, and user-friendly information for a number of applications that have relevance

152   to a broad class of user's decision-making needs, such as in the area of climate change (Wilhelmi

153   et al. 2016). Decision support visualization tools for hydropower planning comprises a unique

154   challenge, in that design considerations for decision making need consider a broad range of data

155   types (e.g. rainfall, streamflow, and power), temporal immediacy (e.g. historical, current

156   observations, forecasts), data source centers (e.g. space agencies and weather centers), the range

157   of temporal scale (e.g. 24-hour, 5-day, 1-month, and 3-month totals) and spatial scale (grid, small-

158   to large-catchment averaging), data accessing formats (e.g. csv, flat file, time-series, etc.),

159   uncertainty information (ensembles versus cumulative probabilities versus averages), and general

160   aesthetic and design considerations.

161   *Objectives of the Study*

162   In this study, the three systems detailed above are combined to create a Decision Support System

163   (DSS) for hydropower planning in Africa and other data scarce regions that leverages the potential

164   of EOS data, ensemble climate forecasts, hydrological models, and stochastic optimization

165   systems.   This study leverages the findings of our previous research to develop, implement, and

166   test a coherent DSS prototype, at daily to seasonal timescales, in a major river basin in Ethiopia

167   consisting of a cascade of hydropower reservoirs. The newly developed DSS contains the

168   following innovations, and web-based tools to enable hydropower managers to implement the DSS

169   in operational settings:

170   • **Selection of appropriate EOS data products** – The DSS includes a new data validation

171   framework for data-scarce regions that allows users to select the best EOS data products,

172   among the wide variety available data products, required for the calibration of climate

173   precipitation forecasts and hydrologic models (Koppa and Gebremichael, 2017). The

174   framework does not require any ground-based data and uses the concept of Budyko

175   hypothesis to select the most appropriate EOS data products that represent the climate

176   accurately and close the water and energy balance.

177   • **Calibration of weather and climate forecasts** – The DSS development has led to

178   innovations in calibrating optimized multi-model/multi-center ensemble weather and

179   climate forecasts at daily (medium-range) and weekly (S2S) time scales using conditioned

180   analogue approaches blended with geostatistical regressors and quantile regression. These

181   post-processsed forecasts then provide skillful and reliable rainfall forecasts tailored for

182   the next stage in hydrometeorological forecast generation.

183   • **Calibration of hydrologic models** – The DSS will use a recently developed Bayesian

184   framework and EOS terrestrial evaporation data product to calibrate a hydrologic model

185   (Koppa, Gebremichael, and Yeh, 2019; Koppa and Gebremichael, 2020). This approach

186   conveniently replaces streamflow data, which is the commonly used data for calibrating

187   hydrologic models, with EOS terrestrial evaporation data products, because most

188   watersheds in Africa are ungauged and even those that are gauged have data quality issues

189   (outdated rating curve, stage measurements observed and recorded manually by non-

190   experts) and availability (substantial time lag until the data are transferred to electronic

191   format and shared by users, and bureaucracy in data sharing).

192   • **Reservoir optimization models** – The DSS will use a new methodology that incorporates

193   uncertainties in climate forecasts and hydrologic model parameters in the optimization of

194   hydropower (Koppa et al. 2019).

195   • **Web-based decision support tool** – A powerful web- and GIS-based visualization tool for

196   analyzing DSS outputs to aid decision makers, that presents information in ways relevant

197   to the unique breadth and challenges of hydropower management.

198 The study is organized as follows. In the next section, we provide a detailed overview of the DSS

199 framework for data scarce regions. Then, we describe the experimental design of the application

200 of the DSS using selected hydropower reservoir systems in Ethiopia as a case study. Finally, we

201 present and discuss the implications of using EOS-based DSS for data scarce regions.

202

203   METHODOLOGY

204   The DSS in this study consists of the following components: a) Earth observations module (EOM),

205   b) Climate forecasting module (CFM), c) Hydrologic forecasting module (HFM), d) Optimization

206   module (OM), and e) Visualization module (VM). The DSS process (Figure 1) starts with the

207   selection of the most appropriate EOS data for precipitation (P) and evapotranspiration (ET)

208   variables for the selected domain (EOM). The selected P dataset is then used to calibrate ensemble

209   weather and climate forecasts using combined analogue and quantile regression approaches

210   (Hopson, 2014; Hopson and Webster, 2010; Knievel *et al.*, 2017; Koenker and Bassett, 1978b) at

211   the daily to seasonal timescales in the CFM. An additional forecast calibration methodology in the

212   form of Bayesian Model Averaging (BMA) (Hoeting *et al.*, 1999; Raftery *et al.*, 2005) is also

213   implemented. Simultaneously, the selected ET dataset is used to calibrate the hydrologic model

214   using a Bayesian calibration algorithm to derive a set of parameters for streamflow forecasting.

215   Next, the calibrated climate forecasts are used as input into the hydrologic model to generate

216   ensemble forecasts of inflows into all the reservoirs in the study domain for the forecast horizon

217   (HFM in Figure 1). In OM, the generated reservoir inflow forecasts are then used as an input into

218   a stochastic programming with recourse model to generate optimized reservoir release decision

219   such that the hydropower production is maximized. Finally, web-based decision support tools

220   visualize the ensemble climate forecasts, the reservoir inflow scenarios, and the optimized release,

221   storage and hydropower decisions (VM in Figure 1). We detail each module of the DSS in the

222   following subsections.

223   Insert Figure 1

224   *Earth Observations Module (EOM)*

225   The primary objective of the EOM is to select the most appropriate EOS-derived P and ET datasets

226   for the calibration of ensemble P forecasts and the hydrologic model. In data scarce regions, such

227   as Africa, evaluation of EOS data products using in-situ measurements is not possible. We use a

228   recently developed framework which does not require in-situ measurements for validating EOS-

229   based P and ET datasets (Koppa and Gebremichael, 2017). The framework compares P and ET

230   datasets against the Budyko hypothesis, a semi-empirical model that describes the coupled water

231   and energy balance of watersheds at long-term timescales (Budyko, 1974), using two indices: (1)

232   Evaporative Index (ET/P, abbreviated as EI) and (2) Aridity Index (PET/P, abbreviated as AI). In

233   the DSS, we utilize Fuh's equation (Fuh, 1981) (Equation 1), a single parameter Budyko function:

234
$$\frac{ET}{P} = 1 + \frac{PET}{P} - \left(1 + \left(\frac{PET}{P}\right)^{\omega}\right)^{\frac{1}{\omega}} \qquad (1)$$

235 where PET is potential ET, and ω is a parameter which has no analytical solution, but several
236 parameterizations have been suggested relating ω to watershed characteristics such as topography,
237 soil, vegetation, and geographical location of watersheds among others (Li et $al.$, 2013; Xu et $al.$,
238 2013).

239 The Budyko curve (Equation 1) is constrained by the following water and energy limits:

240
$$\frac{ET}{P} = 1, \quad \frac{PET}{P} > 1 \qquad (water\ limit) \qquad (2)$$

241
$$\frac{ET}{P} = \frac{PET}{P}, \quad \frac{PET}{P} < 1 \qquad (energy\ limit) \qquad (3)$$

242 The water limit (Equation 2) implies that ET cannot exceed P in the long term. Implicit in the
243 constraint is the assumption that the contribution of watershed storage to long-term water
244 availability is negligible. We note that this assumption may be inadequate in watersheds which
245 have experienced severe long-term groundwater loss (Condon and Maxwell, 2017). In watersheds
246 where water availability is not a constraint, ET is limited by the available energy in the form of
247 net radiation (R_n) or PET (Equation 3). Consequently, in our application of the Fuh equation
248 (Equation 1), the parameter, ω, is stationary. However, several studies have disputed this
249 assumption (Mianabadi et $al.$, 2020; Ning et $al.$, 2018) at finer timescales (monthly, seasonal, or
250 interannual). We acknowledge that the lack of consideration of the non-stationarity in ω could
251 impact the results of the analysis presented below. To reduce this impact, we conduct our analysis
252 at long-term time scales. In addition, we have comprehensively quantified the effect of the
253 variability in ω in a previous study in which we have developed the methodology (Koppa and
254 Gebremichael, 2017). We have shown that at long-term time scale, the value of ω does not have
255 significant on our results. Moreover, similar analysis has been used in a number of hydrological
256 (Greve et $al.$, 2020) and climate change studies (Greve et $al.$, 2014; Zhou et $al.$, 2015). Finally, we
257 emphasize here that a different methodology for selection of precipitation datasets is necessitated
258 by the lack of availability of ground-based measurements for validating the datasets. In regions
259 where such validation datasets are available, the remote sensing datasets should be evaluated using

260 ground-based measurements. As this study focuses on detailing the alternate methodology, we do
261 not present a evaluation with ground-based measurements.

262 In Koppa and Gebremichael (2017), we show that the validation framework is capable of
263 mimicking traditional methodologies which use in-situ measurements. Specifically, we show that
264 the combined error (CE) in P and ET datasets can be represented by the following Euclidean
265 measure (Equation 4):

$$CE = \sqrt{(AI_{est} - AI_{act})^2 + (EI_{est} - EI_{mod})^2} \qquad (4)$$

267 where,

    1) EI_{est} and AI_{est} are the long-term average evaporative and aridity indices estimated from
       satellite-based estimates of P, ET, and R_n considered in this study for water and energy
       balance closure.

    2) AI_{act} is the actual long-term estimate of AI determined using observed R_n from the
       NASA/GEWEX Surface Radiation Budget (SRB) (Cox *et al.*, 2006) v3.0 data and
       precipitation from WorldClim v2.0 dataset (Fick and Hijmans, 2017). This is done as the
       methodology developed in Koppa & Gebremichael (2017) is based on the assumption
       that the aridity of the watershed is known and does not change significantly. The SRB
       data spans the years 1983-2007 with a spatial resolution of 1º x 1º. The temporal range of
       the WorldClim dataset is 1970–2000 and the spatial resolution is 1km x 1km.

    3) EI_{mod} is determined from Fuh's equation (Equation 3) as $EI_{mod} = 1 + AI_{act} -$
       $\left(1 + (AI_{act})^\omega\right)^{1/\omega}$ where ω is the Budyko parameter.

280 As ω has no analytical solution, we use the parameterization developed by (Xu *et al.*, 2013).
281 Specifically, we make use of the following multiple linear regression (MLR) model

$$\omega = 5.057 - 0.093lat + 0.130CTI + 1.316NDVI + 0.000003A - 0.00018elev \qquad (5)$$

283 where,

    1) *lat* is the latitude of the centroid of each watershed. This is derived from the
       HydroBASINS dataset.

286   2) *CTI* is the compound topographic index (Beven and Kirkby, 1979) defined as

287    $\ln(a/\tan\beta)$, where a is the upstream watershed area derived from the HydroBASINS

288   dataset, β is the slope in degrees. We derive the average slope of each watershed from the

289   Multi-Error-Removed Improved-Terrain (MERIT) digital elevation model (DEM) which

290   has coverage of the entire earth (Yamazaki *et al.*, 2017). CTI is correlated with soil

291   moisture. Low CTI values implies smaller watersheds and steep slopes. High CTI values

292   are associated with large watersheds with gentle slopes and represents more water

293   accumulation.

294   3) *A* is the area of watershed derived from HydroBASINS dataset and *elev* is elevation

295   derived from MERIT DEM.

296   4) *NDVI* is the normalized difference vegetation index derived from NASA's Moderate

297   Resolution Imaging Spectroradiometer (MODIS), specifically MOD13A2 v6.0 available

298   at 1km spatial resolution (Didan, 2015). We determine one NDVI value per watershed by

299   averaging over the years 2000–2018.

300   In summary, the following steps are followed to select the best performing P and ET datasets: 1)

301   For a given watershed or catchment area of hydropower reservoirs, the Fuh parameter (ω) is

302   determined using Equation 5. 2) The actual or reference long-term aridity index of the study region

303   is calculated using reliable potential evaporation (PET) or net radiation and precipitation datasets.

304   3) For every combination of P and ET dataset to be evaluated, a Euclidean distance metric in the

305   Budyko space (CE) is calculated using Equation 4. 4) Finally, the combination of P and ET dataset

306   with the least value of CE is selected as the best performing datasets.

307   In the DSS, we implement this framework described above to select the most appropriate P and

308   ET dataset among 14 widely used EOS P and ET datasets (Figure 1 and Table 1), using the

309   Euclidean distance metric described in Equation (4). The best P and ET dataset selected using the

310   framework for a specific watershed will then be used in CFM to calibrate the forecasts and in the

311   HFM to setup and calibrate the distributed hydrologic model.

312   *Climate Forecasting Module (CFM)*

313   In the CFM, weather and climate forecasts at three different timescales can be generated as input

314   to the HFM: daily, sub-seasonal-to-seasonal (S2S), and seasonal. Based on the optimization

315   system, three different forecast scenario structures are produced: a) A single deterministic forecasts

316   for all stages (DET), b) A single deterministic forecast for the first stage and ensemble (stochastic)

317   forecasts for the rest of the forecast horizon (SPWR-D), and c) Ensemble (stochastic) forecasts for

318   all the stages (SPWR-S). For generating these scenarios, raw or calibrated multi-model ensemble

319   weather or climate forecasts are used. Two distinct approaches are available in the CFM for

320   calibration of the forecasts: 1) Combination of analogue and quantile regression, 2) Bayesian

321   Model Averaging (BMA). Below, we provide details of both the approaches.

322   The combined analogue and quantile regression algorithm (Knievel *et al.*, 2017; Koenker and

323   Bassett, 1978) can be explained as follows. Let $\{y_i\}$ represent a set of observations of the

324   regressand y of interest, and $\{\mathbf{x}_i\}$ be an associated set of predictor values. Analogous to standard

325   linear regression, a linear function of $\mathbf{x}$ can be used to estimate to a specific quantile q_θ of y

$$q_\theta(\mathbf{x}_i;\boldsymbol{\beta}) = \beta_0 + \sum_{k=1}^{n} \beta_k x_{ik} + r_i \qquad (6)$$

327   with residuals $r_i = y_i - q_\theta(\mathbf{x}_i;\boldsymbol{\beta})$ and $\theta \in (0,1)$. However, instead of minimizing the squared

328   residuals as with standard linear regression, in QR a weighted iterative minimization of $\{r_i\}$ is

329   performed over $\boldsymbol{\beta}$:

$$\min \sum_{i=1}^{n} \rho_\theta(r_i) = \arg\min_{\beta} \sum_{i=1}^{n} \rho_\theta(y_i - q_\theta(\mathbf{x}_i;\boldsymbol{\beta})), \qquad (7)$$

331   with the weighting function used inside the summation defined as (using a generic placeholder

332   "u"):

$$\rho_\theta(u) = \begin{cases} \theta u & u \geq 0 \\ (\theta-1)u & u < 0 \end{cases}, \qquad (8)$$

334   where the value of θ then prescribes the quantile function that one is solving for (e.g. say, 0.5 for

335   a fit to the median; or 0.9 for a 90th percentile functional fit). The benefits of using QR is that it

336   can be used to estimate the full probability distribution function of the regressand, the optimality

337   of its estimation does not require homoscedastic residuals (unlike standard linear regression), and

338   its functional fit is more immune to unrealistic outliers than standard linear regression (which

339   minimizes the squares of the residuals).

340   Building on this QR backbone, one aspect that makes our postprocessing approach novel is that

341   we "pre-process" the ensemble dispersion ensuring its reliability (Hopson, 2014), and then

342   explicitly condition the training of the final postprocessing model on the degree of the (now-

343   calibrated) ensemble dispersion, the primary benefit of which is that when the ensembles of the

344   forecast are less(more) dispersed, the forecast user can trust that the forecast is more(less) certain.

345   Figure 2 provides a schematic of our approach. Additionally, we have investigated the use of

346   hybrid statistical-dynamical prediction methodologies to multi-model ensemble dynamical

347   forecasts and geophysical teleconnections to generate rainfall predictions. Specifically, at the S2S

348   scale we have enhanced forecast skill of the NCEP-CFSv2 model through combining with Madden

349   Julian Oscillation (MJO) indicators, which we will discuss further below in our Case Study and

350   Results Section.

351   Insert Figure 2

352   The second method implemented for calibration of forecasts is Bayesian Model Averaging

353   (BMA). BMA is a well-established methodology for calibrating forecast ensembles generated

354   from multiple statistical (Hoeting *et al.*, 1999) or dynamical models (Raftery *et al.*, 2005). BMA

355   of a forecast ensemble results in a calibrated and sharp predictive probability density function

356   (PDFs), represented as a weighted averaged of the PDFs of the ensemble members. Following

357   Sloughter *et al.* (2007), the BMA predictive PDF can be mathematically represented as

358   $$P(x|f_1,f_2,...,f_n) = \sum_{n=0}^{N} \omega_n c_n(x|f_n), \qquad (9)$$

359   where ω_n is the posterior probability of ensemble forecast member f_n being the best one,

360   determined in the calibration or training period using observed or reference data of the

361   hydrologic variable under consideration x (for example, precipitation or terrestrial evaporation);

362   and $c_n(x|f_n)$ is the conditional PDF associated with the ensemble forecast f_n of the hydrologic

363   quantity x. For variables such as temperature, the conditional PDF $c_n(x|f_n)$ can be assumed to

364   be normally distributed (Raftery *et al.*, 2005), but a gamma distribution is more appropriate for

365   precipitation (Sloughter *et al.*, 2007). In the DSS, we use a mixture of point mass at zero and a

366   gamma distribution as the conditional PDF (Sloughter *et al.*, 2007). We determine the BMA

367   weights (ω_n) of ensemble precipitation members using the most appropriate P dataset selected in

368   the EOM.

369   In the DSS, we aim to provide support for the most popular global ensemble weather and climate

370   forecasts at daily to seasonal timescales. At daily weather scale (1- to 16-day lead-times), real-

371   time ensemble forecasts are available from NCEP (21 members) and Environment Canada (21

372   ensembles). To expand the multi-model, ensemble forecasts are utilized from an additional six

373   climate centers from the (two-day delayed) THORPEX Interactive Grand Global Ensemble

374   (TIGGE) archive: CMA (15 ensembles), CPTEC (15 ensembles), ECMWF (51 ensembles),

375   MeteoFrance (11 ensembles), UKMet (24 ensembles), and JMA (51 ensembles). The spatial

376   resolutions of the forecasts vary in the range from 0.25 to 1.50 Degrees (Table 1). The forecasts

377   are available at lead times, ranging from nominally 6-hr to 16-days. At the subseasonal- to

378   seasonal-range (S2S; 2- to 6-week lead-times), dynamical real-time forecasts are available from

379   the SubX Project (http://iridl.ldeo.columbia.edu/SOURCES/.Models/.SubX/), with the following

380   contributing models and centers: NCEP-CFSv2, NCEP-GEFS, NASA-GEOS5, ECCC-GEM, US

381   Navy-ESM, NCAR-CCSM4, ESRL-FIM. For seasonal forecasts, we use the North American

382   Multi-Model Ensemble (NMME).*Hydrologic Forecasting Module (HFM)*

383   The main objective of HFM is to generate reliable reservoir inflow forecasts, the primary input to

384   the optimization module. For this, we use the deterministic and stochastic precipitation forecasts

385   at daily to seasonal timescales, produced in the CFM as input into a calibrated spatially distributed

386   hydrologic model. The novel contribution in this module is in the use of terrestrial evaporation

387   (ET) as a proxy for streamflow (SF). The selection of ET as a proxy for SF is motivated by the

388   findings of several previous studies which show that calibrating hydrologic models with ET, in the

389   absence of SF observations, improves the accuracy of SF relative to an uncalibrated model

390   (Immerzeel and Droogers, 2008; López *et al.*, 2017; Zink *et al.*, 2018). Hence, we assume that the

391   high fidelity of the hydrologic model in simulating ET implies accurate simulation of streamflow.

392   In addition, we also introduce the role of hydrologic model parameter uncertainty in affecting the

393   reservoir inflow forecasts and hence hydropower production. For this, we adopt a formal Bayesian

394   calibration approach to derive the posterior probability distribution of model parameters.

395   Specifically, we utilize the Differential Evolution Adaptive Metropolis (DREAM) Markov Chain

396   Monte Carlo Scheme (MCMC) scheme (Vrugt *et al.*, 2008, 2009).

397   First, we calibrate the hydrologic model using the DREAM algorithm to derive the posterior

398   distribution of model errors. Next, we define a limit of acceptability or error threshold to

399   distinguish between behavioral and non-behavioral solutions (Beven, 2006). 'Behavioral'

400   solutions are model parameter sets, derived from calibration, that result in errors that are within an

401   acceptable limit (error threshold) for a specific model output (ET in this study). We use the model

402   parameter set with the least model error for generating deterministic and stochastic inflow

403   scenarios. The remaining behavioral model parameter sets then are used to quantify the uncertainty

404   in ET and SF forecasts due to uncertainty in model parameters. A detailed description of the

405   calibration methodology is available in (Koppa, Gebremichael, and Yeh, 2019).

406   In summary, the following steps are followed in generating the hydrologic forecasts in this module:

407   1) Once the hydrologic model is selected (Noah-MP), the model is calibrated using satellite-based

408   P and ET datasets, 2) The best P and ET datasets selected in the EOM are used in a Bayesian

409   calibration framework (DREAM) to generate a set of behavioral parameters for the hydrologic

410   model (Noah-MP) for the calibration time period (2004), 3) Each set of parameters will result in

411   one set of hydrologic forecast (one ensemble member), 4) The set of parameters are used to

412   generate different deterministic and stochastic inputs to the optimization model (described below).

413   *Optimization Module (OM)*

414   In the OM, we implement a multistage deterministic and stochastic programming with recourse

415   model to optimize hydropower production at the required timescales. First, we provide a generic

416   example of a multistage stochastic programming with recourse model. Then, we describe the

417   specific hydropower optimization scheme implemented in the DSS. We note that the description

418   is provided for seasonal timescales (monthly time step). However, the same optimization scheme

419   is applicable for the daily (hourly time step) to S2S (daily time step) time scales.

420   Consider a system of R reservoirs. Let the seasonal hydropower planning horizon be T months,

421   which is divided into T stages (each stage is one month). Let the monthly time period be

422    $t, t = 1, 2, ...T$. In a multistage stochastic programming with recourse model, at the beginning

423   of each time period t, a reservoir inflow scenario with n scenarios is constructed to represent

424   possible future inflows into the reservoir. These scenario trees or fans are used as an input to an

425   optimization model that minimizes or maximizes the expected value of a specified objective

426   function. We adopt a 'rolling horizon control' scheme in which the optimal release decisions are

427   adopted only for the immediate stage (t). Then, the planning horizon (T) is 'rolled' forward (

428    $t = t + 1$), the reservoir inflows are reforecasted, and the model is re-optimized (recourse). The

429   rolling horizon control is a general-purpose control scheme that involves repeatedly solving a

430   constrained optimization problem, as well as using predictions of future inflows, and constraints

431   over a moving time horizon to choose the control action. This process is repeated until the end of

432   the planning horizon ($t = T$).

433   First, the deterministic and ensemble reservoir inflow forecasts generated in the HFM are used to

434   construct the three scenario structures implemented in the DSS – 1) DET, 2) SPWR-D, and 3)

435   SPWR-S. For the construction of the completely deterministic or DET scenario, only the

436   deterministic forecasts generated from BMA of ensemble precipitation forecasts are used at all

437   stages of the planning horizon (T). As all stages are deterministic, the DET scenario consists of

438   only one inflow scenario. For the SPWR-D scenario, deterministic forecast (from BMA) is used

439   for just the first stage of the planning horizon, and n ensemble forecasts (generated from raw

440   ensemble precipitation forecasts) are used for the remaining $T - 1$ stages (Figure 1). Therefore,

441   SPWR-D scenario consists of n inflow scenarios. Finally, for the SPWR-S scenario, only ensemble

442   forecasts are used at all stages resulting in a completely stochastic scenario, consisting of n

443   scenarios. Note that the DET, SPWR-D, and SPWR-S scenarios are constructed at the beginning

444   of each iteration of the multistage stochastic programming with recourse model, i.e., at each stage

445   t of the planning horizon T. Next, the different scenarios are used as an input to a nonlinear

446   programming (NLP) hydropower optimization model to generate optimal release and storage

447   decisions. We choose NLP because it can accommodate the nonlinear power production functions

448   without approximation. It has been shown that NLP models are most accurate in generating reliable

449   release and storage policy for reservoir management and operation (Barros *et al.*, 2003). A detailed

450   description of the optimization methodology is available in Koppa, Gebremichael, Zambon, *et al.*

451   (2019).

452   In summary, the following steps constitute the optimization module: 1) Rolling horizon scheme is

453   followed in which the system is optimized at the start of every month for a planning horizon of 8

454   months, 2) A the start of every month, three inflow scenarios (DET, SPWR-D, and SPWR-S) are

455   generated 3) DET is generated by combining the BMA of precipitation forecasts (CFM) with the

456   Noah-MP model run with the best parameter set from HFM for all the 8 months, 4) SPWR-D is

457   generated by running the BMA forecast through the Noah-MP model for the first month, and for

458 the remaining months all the ensemble climate forecasts and parameter sets are used to generate

459 an ensemble of forecasts for the remaining 7 months , 5) SPWR-S scenario is generated using

460 ensemble forecasts and model parameters for all the, 6) The system is optimized for the entire 8

461 months, but the decisions are implemented only for the first month, 7) At the start of the next

462 month, the entire procedure (Step 1 -7) is repeated for the next months.

463 *Visualization Module (VM)*

464 Because each collaboration has its own region with its own unique geography, hydrology, and

465 decision-making needs, each partnership begins by identifying the relevant datasets, and forecast

466 models, as well as determining the most convenient output formats, including spatial requirements

467 (local catchments, grids or sites) and best data formats for interfacing with the agencies' current

468 prediction systems. Because of this, the VM is primarily oriented around a customizable web-

469 based decision support tool that integrates many of the outputs from the DSS into a GIS-based

470 visualization framework to aid decision makers in assessing and downloading the DSS data outputs

471 into their particular context. The power behind the VM is the ability to visualize and interrogate

472 the output from the DSS through space and time. A time series graph of precipitation estimates for

473 each catchment is integrated into the interactive mapping application for each catchment. The

474 democratization of the forecasts lead to enhanced situational awareness of possible future rainfall

475 events for decision makers. The web application components are built using open source data

476 formats, programming languages, and, mapping and graphing libraries.The spatial forecast data is

477 stored as a JavaScript Object Notation (JSON) file, which is a standard for storing and exchanging

478 data written in JavaScript notation, while the time series for each catchment is stored as Common

479 Seperated Values (CSV) files. the webapplication is developed using JavaScript code libraries;

480 the mapping component uses a library called Leaflet (Leaflet, 2016), while the time series are

481 plotted using the JQPlot. Leaflet is one of the most popular mapping JavaScripts libraries today

482 (Donohue *et al.*, 2013) and is used as the mapping engine to glue all map and data services together.

483 The data services that are displayed in the VM are spatial and temporal aggregations of

484 precipitation estimates from the EOSs and CFMs. This aggregation is developed using Python

485 scripting and the open-source library called GDAL/OGR. The processing steps required for our

486 precipitation product displays are provided in Figure 3.

487   Insert Figure 3

489   As described in the previous section, the DSS developed in this study contains several components

490   to aid in the generation of reliable reservoir release decisions at different timescales (daily to

491   seasonal). The components include consideration of various EOS-based P and ET datasets (14

492   datasets), ensemble climate forecasts, hydrologic models (based on NASA's LIS), uncertainty

493   quantification (incorporation of model parameter uncertainty in addition to climate forecasts

494   uncertainty), different optimization schemes (deterministic or stochastic), and visualization

495   support tool design considerations. However, for the purpose of the case study, we apply a specific

496   sequence of the DSS chain for a large river basin in East Africa at seasonal timescales: a) In the

497   EOM, we use all the EOS-based datasets described in Table 1; b) In the CFM, we use the NMME

498   seasonal forecasts to generate all the three different scenarios (DET, SPWR-D, and SPWR-S) to

499   couple to the HFM, and use NCEP and TIGGE forecasts for daily to weekly rainfall guidance; c)

500   In the HFM, we setup the Noah-MP hydrologic model (Niu *et al.*, 2011) using NASA's LIS and

501   calibrate the model using DREAM, however, we select only one behavioral parameter set and

502   therefore no model parameter uncertainty is incorporated in the final release decision; d) In the

503   OM, we use deterministic and stochastic programming model at monthly timestep to optimize

504   hydropower under DET, SPWR-D, and SPWR-S scenarios. In the following sections, we present

505   the hydropower scheme selected as a case study, describe implementation of the developed

506   methodology step-by-step, demonstrate the added value of the DSS by comparing results against

507   actually generated hydropower values, and present the particular implementation of our

508   visualization and support module for the DSS.

509   *Study Area and Time Period*

510   Our study region is the Omo-Gibe river basin, with an area of 79,000 km^2, in Ethiopia (Figure 4).

511   The elevation ranges from about 700 to 3,100 m.a.s.l. The average rainfall in the basin is about

512   1,150 mm with a humid north and arid south. The annual temperature varies between 17 ^{o}C and

513   29 ^{o}C. The study area consists of three power plants in operation (Gilgel Gibe I, II and III) and one

514   planned hydropower plant (Koysha) – see Table 2 for characteristics of the hydropower plants.

515   For our study, we considered a cascade of two reservoirs (Gibe I and Gibe III). We focused on the

516   time period of February 2005 to September 2005, due to availability of actually generated

517   hydropower production data. Assuming a planning horizon of eight months, we forecasted inflows

518   to the reservoirs eight months in advance. Therefore, this case study demonstrates the values of

519   our DSS when we selected forecasts made eight months in advance.

520   Insert Figure 4

521   *Earth Observations Datasets (EOS)*

522   The first step in implementing the DSS is the selection of an appropriate EOS-based P and ET

523   datasets required for the calibration of climate forecasts and the calibration of the hydrologic

524   model. Using the Budyko-based framework of the DSS (see EOM component in Fig. 1), we select

525   the most appropriate P and ET datasets from a list of fourteen datasets (Table 1) in the following

526   steps. We discretize the study domain into regular grids of 0.25º x 0.25º (a total of 592 grids). The

527   14 datasets are then interpolated onto the grids using bi-linear interpolation. For each of the grid,

528   the Budyko parameter is calculated using Equation 5. Then the combined error (CE) in a

529   combination of P and ET dataset (total of 49 combinations) is determined for each grid cell using

530   Equation 4. Finally, the Root Mean Square Error (RMSE) of all the CE values (total of 592 values)

531   is used to summarize the performance of a specific combination of P and ET in representing the

532   water and energy balance of the Omo-Gibe river basin. The combination of P and ET dataset with

533   the least RMSE is selected as the best combination. In Figure 5, we present a heat map of the

534   RMSE of each combination of P and ET dataset. It is seen that the best combination of P and ET

535   dataset (i.e. with the least RMSE) is obtained for the P product "PERSIANN.CDR" and ET product

536   "SSEBOpv4.0".

537   Insert Figure 5

538   *Weather and Seasonal Precipitation Forecast Data*

539   For climate forecasts, we use the ensemble seasonal precipitation forecasts from the North

540   American Multi-model Ensemble (NMME) (Kirtman *et al.*, 2014). It consists of nine partner

541   models with the number of ensemble members in each model varying from six to twenty-eight.

542   As the hydrologic model (described below) requires daily forecasts to run, three models which

543   provide the seasonal forecasts at daily time step are chosen : 1) Goddard Earth Observation

544   System version 5 (GEOS-5) (Borovikov *et al.*, 2019), 2) Third generation Canadian Coupled

545   Global Climate Model (CanCM3) (Merryfield *et al.*, 2013), and 3) Fourth generation Canadian

546   Coupled Global Climate Model (CanCM4) (Merryfield *et al.*, 2013). The CanCM3 and CanCM4

547   models issue forecasts for lead times of up to 12 months. GEOS-5 forecasts are available for lead

548   times of up to 9 months. With ten ensemble members for each model, the DSS application to the

549   Omo-Gibe river basin uses a total of thirty ensembles from three models. The hindcasts of

550   NMME are available for the time period 1981-2010. The spatial resolution is 1.0° x 1.0° and the

551   temporal resolution is daily.

552   At the daily- to two week-range time-scales, the dynamical forecast products we discussed above

553   are used to provide rainfall guidance to the user, with these forecasts coming from NCEP and

554   TIGGE. For S2S forecasts, geostatistical information at weekly-evolving time-scales can also be

555   used to enhance NWP rainfall forecasting skill. In Figure 6, we show composite plots of how the

556   Madden-Julian Oscillation (MJO) impacts rainfall anomalies over Ethiopia based on the phase of

557   the MJO because of its proximity to the equator (Broman, 2019).

558   Insert Figure 6

559   Similarly, at seasonal timescales, ENSO can have an impact on the rainfall over the major river

560   basins in Ethiopia, but the phase of the impact varies strongly based on the location, as we see in

561   Figure 7.

562   Insert Figure 7

563   *Hydrologic Model Setup and Calibration*

564   To translate the NMME precipitation forecasts into reservoir inflow forecasts, we choose the

565   Noah-MP (Multi-Parameterization) Land Surface Model (LSM) (Niu *et al.*, 2011), driven through

566   NASA's Land Information System (LIS) (Kumar *et al.*, 2006). We source the static input datasets

567   required   for   running   the   Noah-MP   mode   from   NASA's   LIS   data   portal

568   (https://portal.nccs.nasa.gov/lisdata). This includes the land cover map, sourced from United

569   States Geological Survey (USGS); the soil texture map from State Soil Geographic (STATSGO)

570   dataset, sourced from the United States Department of Agriculture (USDA); and the elevation map

571   from GTOPO30, sourced from USGS. Albedo, greenness fraction and temperature are sourced

572   from the National Centers for Environmental Prediction (NCEP) reanalysis. The meteorological

573   forcings required by the Noah-MP model include precipitation, air temperature, surface pressure,

574   specific humidity, wind speed, and radiation. Barring PERSIANN.CDR precipitation, all

575   meteorological forcings are derived from the Global Data Assimilation System (GDAS), sourced

576 from the Environmental Modeling Center (EMC) of the NCEP. The spatial resolution of the dataset

577 is 0.47° x 0.47°. The Noah-MP model is set at a spatial resolution of 5km x 5km. The

578 meteorological inputs, including the forecasts, are interpolated onto the model grid using bilinear

579 interpolation. The model is spun-up for a period of 68 years by looping through the year 2003 until

580 the groundwater and soil moisture storage reach equilibrium. The model time step is three hours.

581 The number of soil layers in the model is four with thicknesses 10cm, 30cm, 60cm, and 100cm.

582 Specific Noah-MP model physics options selected for different processes are detailed in Table 3.

583 The Noah-MP model contains 71 standard parameters (present in user-defined tables) and 139

584 hard-coded parameters (present in the model code). The Noah-MP model output has been found

585 to be sensitive to about two-thirds of the 71 standard parameters (Cuntz *et al.*, 2016). We select

586 five of the most sensitive parameters from the Cuntz *et al.* (2016) study. The selected parameters

587 are two surface runoff-related parameters (REFDK and REFKDT), the exponent in the Brooks-

588 Corey equation (BB), soil porosity (MAXSMC), and hydraulic conductivity at saturation

589 (SATDK). Of the five parameters, BB, MAXSMC, and SATDK are related to soil texture. As

590 there are twelve soil texture classes, the total number of parameters selected for calibration of the

591 Noah-MP hydrologic model is 38 (Table 4 presents a detailed breakdown of the parameters with

592 maximum and minimum values used for calibration).

593 To calibrate the hydrologic model and quantify the uncertainty in reservoir inflow forecasts due to

594 uncertainty in model parameters, we use the DREAM algorithm. Specific configuration options

595 and parameters of the DREAM algorithm used in this study are detailed in Table 5. In the absence

596 of streamflow observations, we use satellite-based estimates of ET (SSEBOpv4.0) to calibrate the

597 hydrologic model for the year 2004. Specifically, error residuals are determined at all the 5km x

598 5km grid cells and time steps (monthly) over the entire Omo-Gibe River basin. On a workstation

599 with 24 processors, DREAM required approximately 11,300 iterations to converge to a solution.

600 For the purpose of this case study, we choose the best performing model parameter. As described

601 in the methodology section, multiple behavioral solutions from DREAM can be used to

602 incorporate model parameter uncertainty in hydropower decision making. A comprehensive

603 quantification of model parameter uncertainty and its impact on hydropower is discussed in Koppa,

604 Gebremichael, Zambon, *et al*. (2019).

605 *Visualization Module*

606 Our visualization module provides displays and downloadable data of rainfall estimates from

607 forecasts at time-scales of short-, medium-, and seasonal-range over East Africa, with focus over

608 Ethiopia. Spatially, to provide the viewer with different scales of resolution, two different sizes of

609 basin-averaged rainfall were provided on the displays, which the user could access through zoom-

610 in and zoom-out features. The chosen catchment scales are shown in Figure 8.

611   Insert Figure 8

612   RESULTS AND DISCUSSIONS

613 First, we evaluate the weather and seasonal precipitation hindcasts over our case study region, the

614 Omo-Gibe river basin, and the major basins of Ethiopia. Then, we evaluate the Noah-MP

615 hydrologic model using ET estimates from SSEBOpv4.0. Next, we present the reservoir inflow

616 forecasts and resulting three different scenario structures used for optimization. We also present

617 the results from the deterministic and stochastic programming with recourse model including the

618 optimized release decisions and resulting hydropower production. Finally, we show results from

619 our developed Visualization Module.

620 *Evaluation of Weather and Climate Forecasts*

621 To validate the 30-member seasonal ensemble precipitation forecasts from NMME, we use the

622 PERSIANN-CDR dataset (selected in the EOM). We present Taylor diagrams (Taylor, 2001) to

623 represent the root mean square error (RMSE), correlation with observations and standard deviation

624 of different forecast models (Figure 9). A Taylor diagram represents the standard deviation of the

625 observed data and modeled results, radially, along the x and y axes (for example the standard

626 deviation of the observed precipitation is approximately 50 mm). The correlation of the different

627 models with the observed data is shown along the circumference of the Taylor diagram, increasing

628 radially from the y-axis to the x-axis (for example, the observed data is shown on the x axis,

629 representing a correlation of 1.0 and CanCM4 has a correlation of 0.92 at lead time of 1-month).

630 Finally, the RMSE of models are represented as contours (dashed yellow lines in Figure 4), with

631 RMSE values increasing from the x-axis to y-axis (for example, the observed data is shown on the

632 x-axis, representing an RMSE of 0.0 and CanCM4 has an RMSE of approximately 20 mm/month

633 at lead time of 1-month). The closer the point representing a model (for example, CanCM4) is to

634 the observed data (purple point in Figure 5), better the performance of the model.

635 The stochastic programming with recourse model implemented in this study uses forecasts that are
636 updated at the start of each month, while the release decisions are implemented only for the
637 immediate stage. Therefore, we focus on the performance of the forecasts at shorter lead times. At
638 lead times of 2-3 months, we see that the GEOS-5 model consistently outperforms the other two
639 models (Figure 9). At lead time of 1-month, the CanCM4 model exhibits lower RMSE and higher
640 correlation with the observed data (Figure 9). However, at longer lead times, CanCM4 model
641 performs relatively poorly compared with the other models. As expected, the forecast accuracy of
642 all the models deteriorates with increasing lead times.

643 Finally, we compare the simple mean and Bayesian model average of all 30 ensemble members
644 with the individual models. We see that the ensemble BMA outperforms all the other models at
645 almost every lead time (Figure 9). The low RMSE (approximately 18 mm/month) and high
646 correlation coefficient (greater than 0.9) at lead time 1-month supports this conclusion. At shorter
647 lead times, the CanCM4 model outperforms the ensemble mean in terms of both the magnitude of
648 error and correlation with the observed data. This highlights the advantage of the BMA technique,
649 which provides higher weights to better performing models (CanCM4 in this case). The ensemble
650 mean, which weighs all the ensemble members equally, is biased by the lower performing
651 CanCM3 and GEOS-5 models.

652   Insert Figure 9

653 The inclusion of large-scale teleconnections as geostatistical predictors along with NWP multi-
654 modeling can greatly enhance the forecasting skill of NWP seasonal and weather forecasts over
655 not only over the Omo-Gibe river basin (our primary study region), but over all the major river
656 basins of Ethiopia. Building on the relationship between ENSO and rainfall anomalies shown in
657 Figure 7 above, in Figure 10 we utilize ENSO as a predictor along with all eight NMME models
658 into an optimized probabilistic forecast for the Blue Nile river basin, using the Centennial Trends
659 (CenTrends) gauge-based precipitation dataset (Funk, Nicholson, *et al.*, 2015) for observations.
660 The individual forecast models are calibrated using a regression of the model ensemble mean
661 against the observations leaving one year out at a time (Unger *et al.*, 2009). A simple linear
662 regression is also used to create a probabilistic forecast based on the Nino3.4 index. A multi-
663 model forecast is then calculated by averaging the individual NMME forecasts together with
664 ENSO. Since the higher confidence forecasts show greater variability from the climatological

665   mean, they will be more highly weighted in the average. As a last step, the output of the multi-

666   model forecast itself is once again calibrated to ensure accurate forecast probabilities. The

667   summer season rainfall over the basin can be skillfully forecast using this multi-model approach

668   (*R=0.59, p<0.001*).

669   Insert Figure 10

670   Similarly, geostatistical information at weekly-evolving time-scales can also be used to enhance

671   NWP rainfall forecasting skill. Utilizing the information shown in Figure 6 on how the phasing of

672   the MJO impacts rainfall anomalies over Ethiopia, this information, along with NWP rainfall

673   forecasts from NCEP's CFSv2, can be combined through a quantile regression model, to

674   significantly improve weekly time-scale rainfall forecasts for the Omo-Gibe, as shown in Figure

675   11 (Broman *et al.*, 2020) .

676   Insert Figure 11

677   At daily-to-two-week time-scales, combining NWP ensemble forecasts into a multi-model forecast

678   can provide significant benefits in forecasting skill for extreme events, as we show below in Figure

679   12 (here, 90th percentile rainfall), where we compare rainfall forecasting skill of four weather

680   centers (Canada – CMC, ECWMF, US – NCEP, UK Met Office) to a combined multi-model over

681   Ethiopia (Stellingwerf et al., 2020). As shown in the figure using the Brier skill score, the multi-

682   model forecast is equal to or out-performs any individual model for all of the 12 primary Ethiopian

683   river basins shown.

684   Insert Figure 12

685   *Evaluation of Hydrologic Model Calibration and Reservoir Inflow Forecasts*

686   We validate the set of selected behavioral solutions with the SSEBOpv4.0 ET dataset for the year

687   2005 using time series (Figure 13a) and relevant error metrics. Figure 13a reveals that the

688   SSEBOpv4.0 ET-calibrated Noah-MP model performs well in simulating ET over the Omo-Gibe

689   River basin. In the calibration period (12 months of 2004), we see that the reference ET data (black

690   line) is closer to the 5% quantile of the modelled ET for the months of April, May, and June. This

691   implies that the behavioral solutions consistently overestimate ET for the months with higher

692   observed evapotranspiration. In the validation period (12 months of 2005), the reference dataset

693 corresponds to the median modelled ET values for the first six months. In this last six months of

694 2005, we see that the model consistently underestimates ET over the study area. Additionally, the

695 model can capture the quantity and timing of the peaks and troughs seen in the reference ET

696 dataset. A low mean RMSE of 2.5 mm/month and a high mean correlation co-efficient of 0.94,

697 determined for the validation time period, shows that the Noah-MP model is capable of simulating

698 ET. As stated in the methodology, we assume that the high fidelity of the Noah-MP model in

699 simulating ET across the Omo-Gibe River basin implies accurate simulation of streamflow.

700 For the application of the DSS in the Omo-Gibe river basin, we select the best performing Noah-

701 MP model parameter set from the twenty behavioral solutions (used in Figure 13a) to generate the

702 reservoir inflow forecasts for two reservoirs (Gibe I and Gibe III). As described in the

703 methodology, we construct three scenario structures (DET, SPWR-D, and SPWR-S) for the

704 months February 2005 to September 2005 by combining the calibrated and uncalibrated NMME

705 precipitation forecasts and the ET-calibrated Noah-MP hydrologic model. Here, we compare the

706 differences in reservoir inflows among the three scenarios. Figure 13b presents the deterministic

707 (from BMA) and stochastic (raw forecast ensembles) inflows used to construct the three scenario

708 trees. In addition, we also present the inflows generated from a climatological forecast generated

709 by forcing Noah-MP with PERSIANN-CDR precipitation for a period of 10 years (2002 – 2015)

710 (SEASN) and determining the average streamflow values for each month of the planning horizon.

711 We see that the first three months of the study period are relatively dry compared to the rest of the

712 months. Also, the deterministic inflows into both Gibe I and Gibe III are near the mean of the 30-

713 member ensemble, with July and September being the exceptions. Additionally, we also see that

714 there is considerable uncertainty in the reservoir inflow arising from uncertainty in the input

715 precipitation ensembles (boxplots in Figure 13b). The climatological forecasts are higher than the

716 mean of the ensemble mean in the low flow months and lower than the ensemble mean in the high

717 flow months.

718   Insert Figure 13

719 *Optimized Release Decision and Power Produced*

720 The three inflow scenarios (DET, SPWR-D, and SPWR-S) along with the climatological forecast

721 generated using 10-year of PERSIANN-CDR data (SEASN) are used as inputs to a deterministic

722   and stochastic programming with recourse model to generate optimized power releases (Figure

723   14a) and the associated hydropower production (Figure 14b).

724   For the Gibe I reservoirs, we see that the release decisions generated with the DET and SPWR-D

725   inflow scenario structures are similar to each other, except for the month of May 2005 (Figure

726   14a). We note here that the results correspond to the immediate stage of the stochastic

727   programming with recourse model. Therefore, the similarity between the DET and SPWR-D

728   release decisions may be because the immediate stage of the SPWR-D model is deterministic,

729   and the value derived from BMA of ensemble members is equal to the DET inflow scenario

730   structure. We see that the optimized release decisions are consistently higher in the SPWR-S

731   case compared with either the DET or SPWR-D scenario structures, in the dry months. However,

732   in the later months of the planning horizon the releases are lower. In Gibe III, the SPWR-S

733   scenario is consistently higher than the DET or SPWR-D scenarios for all months. Additionally,

734   for Gibe 3, it is interesting to note that the uncertainty in the inflows represented in the SPWR-S

735   scenarios only impacts the dry periods (February 2005 to May 2005). In the wet months, the

736   power releases reach the capacity of the power plants.

737   Finally, we compare the optimized hydropower values with the actual power produced at the

738   Gibe I reservoir for the months of February 2005 to September 2005. Due to unavailability of

739   historic hydropower production data, we do not present the same comparison for Gibe III

740   reservoir. The actual power produced in Gibe I for the eight-month study period is 0.53 million

741   MWh. In comparison, the optimized hydropower generated from the DET, SPWR-D, and

742   SPWR-S scenario structures are 0.68 million MWh, 0.71 million MWh, and 0.76 million MWh

743   respectively (Table 6). The higher power produced in the SPWR-S scenario structure may be

744   attributed to the consistently higher values of reservoir inflow compared with the DET and

745   SPWR-D scenarios. We note that reservoir evaporation has been ignored in our study, which,

746   when included, may reduce the optimized hydropower values. To avoid this bias, we compare

747   the power production results of the three reservoir inflow scenarios with a baseline scenario

748   generated with climatology (SEASN). The hydropower generated from the climatological inflow

749   forecasts in Gibe I is approximately 0.54 million MWh. In comparison, all the different scenarios

750   (DET, SPWR-D, and SPWR-S) represent a significant improvement in terms of power

751   production. In Gibe III, the power produced from DET, SPWR-D, SPWR-S scenarios are 1.96,

752   1.96, and 2.1 million MWh respectively. The power produced from the climatological inflow

753   forecast is approximately 1.84 million MWh (Table 6).

754   Insert Figure 14

755   *Visualization Module for Decision Support System*

756   Our developed Visualization Module for the dissemination of real-time and automated climate

757   data is shown below in Figure 15, which shows a screenshot of the current display and user

758   interface. The interactive nature of the VM is the power behind the DSS. The selection options

759   on the left-hand side of the map provide the following options: The choice to display satellite

760   products verses forecast precipitation estimates; the selection of a temporal averaging period (24-

761   hr, 5-day for satellite and 24-hr, 5-day, 1 month, 3 month for forecast estimates); a temperal period;

762   and the satellite product, forecast model or a merged/multi-model product. Once the data is

763   mapped different spatial scales for the catchments are available through the zoom-in functionality,

764   and a time series plot is displayed through the click functionality on a catchment. Finally, the data

765   from the time series is available as a download into a text file format.

766   Insert Figure 15

767

768   CONCLUSIONS, LIMITATIONS, AND FUTURE WORK

769   In this study, we presented a novel decision support system (DSS) to aid hydropower planning

770   from daily to seasonal timescales in Africa, where significant increases in hydropower capacity is

771   hindered by lack of reliable data. The DSS demonstrates how the progress in earth observation

772   satellites, ensemble weather and climate forecasts, and distributed large scale hydrologic

773   modelling can be leveraged to create an implementable tool for helping water managers take

774   reliable decisions under deep uncertainty. The DSS applied to a real hydropower system in East

775   Africa resulted in significant improvements over both the current hydropower production (34%)

776   and a system optimized using climatological forecast (20%). The DSS is flexible enough to provide

777   the decision makers with several different options ranging from different EOS-based data products

778   and multiple hydrologic models (enabled by NASA's Land Information System) to different

779   scenario structures to account different sources of uncertainty. To the authors' knowledge, this is

780   the first demonstration of a DSS for hydropower optimization at seasonal timescales using earth
781   observation satellites and dynamical forecasts.

782   During the course of the design of the DSS, we have made sure that all the components which
783   form the overall framework are not only open source but are proven in several hydrologic and
784   water resources applications by different research communities over the recent decades. This
785   includes the satellite-based remote sensing datasets, the hydrologic model and the optimization
786   system. However, we acknowledge that there are several other alternative datasets are models
787   which could be equally suitable for producing accurate hydrologic forecasts and improved
788   hydropower in data-scarce regions. For example, simpler frameworks which combine runoff from
789   downscaled global scale seasonal climate forecast systems such as SEAS5 (Johnson *et al.*, 2019)
790   with offline routing schemes such as the Routing Application for Parallel computation of
791   Discharge (RAPID) (David *et al.*, 2011) have shown promise (Snow *et al.*, 2016). Global
792   hydrological forecast systems such as the Global Flood Awareness System (GloFAS) (Alfieri *et*
793   *al.*, 2013) are also an plausible alternative. A comprehensive DSS intercomparison studies, like
794   the ones in the climate modeling community (Eyring *et al.*, 2016), would help water managers
795   decide the best structure of DSS suitable for their specific applications.

796   As the structure of the DSS is modular, it can form the basis for further improvements which can
797   overcome the limitations of the prototype framework presented here. Prior to the application of the
798   DSS in an operational mode, it must be tested comprehensively in a data-rich study region,
799   although we note that issues of transferability will always remain. We envisage a similar DSS for
800   multi-purpose reservoirs that considers additional EOS-observations for calibration of hydrologic
801   models including total water storage from the Gravity Recovery and Climate Experiment
802   (GRACE) satellites, soil moisture from the Soil Moisture Active Passive (SMAP) mission, and
803   even direct discharge measurements from the upcoming Surface Water and Ocean Topography
804   (SWOT) mission.

805

806   ACKNOWLEDGEMENTS

810

811   Literature Cited

812 Alemu, E.T., R.N. Palmer, A. Polebitski, and B. Meaker, 2011. Decision Support System for

813   Optimizing Reservoir Operations Using Ensemble Streamflow Predictions. Journal of

814   Water Resources Planning and Management 137:72–82.

815 Alfieri, L., P. Burek, E. Dutra, B. Krzeminski, D. Muraro, J. Thielen, and F. Pappenberger, 2013.

816   GloFAS - Global Ensemble Streamflow Forecasting and Flood Early Warning. Hydrology

817   and Earth System Sciences 17:1161–1175.

818 Ashouri, H., K.-L. Hsu, S. Sorooshian, D.K. Braithwaite, K.R. Knapp, L.D. Cecil, B.R. Nelson,

819   O.P. Prat, H. Ashouri, K.-L. Hsu, S. Sorooshian, D.K. Braithwaite, K.R. Knapp, L.D. Cecil,

820   B.R. Nelson, and O.P. Prat, 2015. PERSIANN-CDR: Daily Precipitation Climate Data

821   Record from Multisatellite Observations for Hydrological and Climate Studies. Bulletin of

822   the American Meteorological Society 96:69–83.

823 Barros, M.T.L., F.T.-C. Tsai, S. Yang, J.E.G. Lopes, and W.W.-G. Yeh, 2003. Optimization of

824   Large-Scale Hydropower System Operations. Journal of Water Resources Planning and

825   Management 129:178–188.

826 Benninga, H.-J.F., M.J. Booij, R.J. Romanowicz, and T.H.M. Rientjes, 2017. Performance of

827   Ensemble Streamflow Forecasts under Varied Hydrometeorological Conditions. Hydrology

828   and Earth System Sciences 21:5273–5291.

829 Beven, K., 2006. Searching for the Holy Grail of Scientific Hydrology: Qt=(S, R, Δt)A as

830   Closure. Hydrology and Earth System Sciences 10:609–618.

831 Beven, K.J. and M.J. Kirkby, 1979. A Physically Based, Variable Contributing Area Model of

832   Basin Hydrology. Hydrological Sciences Bulletin 24:43–69.

833 Bitew, M.M., M. Gebremichael, L.T. Ghebremichael, and Y.A. Bayissa, 2012. Evaluation of

834   High-Resolution Satellite Rainfall Products through Streamflow Simulation in a

835   Hydrological Modeling of a Small Mountainous Watershed in Ethiopia. Journal of

836   Hydrometeorology 13:338–350.

837   Borovikov, A., R. Cullather, R. Kovach, J. Marshak, G. Vernieres, Y. Vikhliaev, B. Zhao, and Z.

838   Li, 2019. GEOS-5 Seasonal Forecast System. Climate Dynamics. doi:10.1007/s00382-017-

839   3835-2.

840   Broman, D., B. Rajagopalan, T. Hopson, and M. Gebremichael, 2020. Spatial and Temporal

841   Variability of East African Kiremt Season Precipitation and Large-scale Teleconnections.

842   International Journal of Climatology 40:1241–1254.

843   Budyko, M.I. (Mikhail I., 1974. Climate and Life. Academic Press.

844   https://books.google.co.in/books/about/Climate_and_Life.html?id=Ln89Y-

845   6KwZYC&redir_esc=y. Accessed 14 Oct 2019.

846   Condon, L.E. and R.M. Maxwell, 2017. Systematic Shifts in Budyko Relationships Caused by

847   Groundwater Storage Changes. Hydrology and Earth System Sciences 21:1117–1135.

848   Conway, D., C. Dalin, W.A. Landman, and T.J. Osborn, 2017. Hydropower Plans in Eastern and

849   Southern Africa Increase Risk of Concurrent Climate-Related Electricity Supply Disruption.

850   Nature Energy 2:946–953.

851   Cox, S.J., P.W. Stackhouse Jr, S.K. Gupta, J.C. Mikovitz, T. Zhang, L.M. Hinkelman, M. Wild,

852   and A. Ohmura, 2006. The NASA/GEWEX Surface Radiation Budget Project: Overview

853   and Analysis. Extended Abstracts, 12th Conf. on Atmospheric Radiation.

854   Crow, W.T. and D. Ryu, 2009. A New Data Assimilation Approach for Improving Runoff

855   Prediction Using Remotely-Sensed Soil Moisture Retrievals. Hydrology and Earth System

856   Sciences 13:1–16.

857   Cuntz, M., J. Mai, L. Samaniego, M. Clark, V. Wulfmeyer, O. Branch, S. Attinger, and S.

858   Thober, 2016. The Impact of Standard and Hard-Coded Parameters on the Hydrologic

859   Fluxes in the Noah-MP Land Surface Model. Journal of Geophysical Research.

860   doi:10.1002/2016JD025097.

861   Cuo, L., T.C. Pagano, and Q.J. Wang, 2011. A Review of Quantitative Precipitation Forecasts

862   and Their Use in Short- to Medium-Range Streamflow Forecasting. Journal of

863   Hydrometeorology 12:713–728.

864   David, C.H., D.R. Maidment, G.Y. Niu, Z.L. Yang, F. Habets, and V. Eijkhout, 2011. River

865   Network Routing on the NHDPlus Dataset. Journal of Hydrometeorology.

866   doi:10.1175/2011JHM1345.1.

867   Didan, K., 2015. MOD13C1 MODIS/Terra Vegetation Indices 16-Day L3 Global 0.05Deg CMG

868   V006. EOSDIS Land Processes DAAC.

869   Donohue, R.G., C.M. Sack, and R.E. Roth, 2013. Time Series Proportional Symbol Map with

870   Leafet and Jquery. Cartographic Perspectives. doi:10.14714/CP76.1248.

871   Etkin, D., P. Kirshen, D. Watkins, C. Roncoli, M. Sanon, L. Some, Y. Dembele, J. Sanfo, J.

872   Zoungrana, and G. Hoogenboom, 2015. Stochastic Programming for Improved Multiuse

873   Reservoir Operation in Burkina Faso, West Africa. Journal of Water Resources Planning

874   and Management 141:04014056.

875   Eyring, V., S. Bony, G.A. Meehl, C.A. Senior, B. Stevens, R.J. Stouffer, and K.E. Taylor, 2016.

876   Overview of the Coupled Model Intercomparison Project Phase 6 (CMIP6) Experimental

877   Design and Organization. Geoscientific Model Development. doi:10.5194/gmd-9-1937-

878   2016.

879   Fick, S.E. and R.J. Hijmans, 2017. WorldClim 2: New 1-Km Spatial Resolution Climate

880   Surfaces for Global Land Areas. International Journal of Climatology 37:4302–4315.

881   Fletcher, S., M. Lickley, and K. Strzepek, 2019. Learning about Climate Change Uncertainty

882   Enables Flexible Water Infrastructure Planning. Nature Communications 10:1–11.

883   Fuh, B., 1981. On the Calculation of the Evaporation from Land Surface. Scientia Atmospherica

884   Sinica 5:23–31.

885   Funk, C., S.E. Nicholson, M. Landsfeld, D. Klotter, P. Peterson, and L. Harrison, 2015. The

886   Centennial Trends Greater Horn of Africa Precipitation Dataset. Scientific Data.

887   doi:10.1038/sdata.2015.50.

888   Funk, C., P. Peterson, M. Landsfeld, D. Pedreros, J. Verdin, S. Shukla, G. Husak, J. Rowland, L.

889   Harrison, A. Hoell, and J. Michaelsen, 2015. The Climate Hazards Infrared Precipitation
890   with Stations—a New Environmental Record for Monitoring Extremes. Scientific Data
891   2:150066.

892   Greve, P., P. Burek, and Y. Wada, 2020. Using the Budyko Framework for Calibrating a Global
893   Hydrological Model. Water Resources Research 56. doi:10.1029/2019wr026280.

894   Greve, P., B. Orlowsky, B. Mueller, J. Sheffield, M. Reichstein, and S.I. Seneviratne, 2014.
895   Global Assessment of Trends in Wetting and Drying over Land. Nature Geoscience 7:716–
896   721.

897   Griggs, D., M. Stafford-Smith, O. Gaffney, J. Rockström, M.C. Öhman, P. Shyamsundar, W.
898   Steffen, G. Glaser, N. Kanie, and I. Noble, 2013. Policy: Sustainable Development Goals
899   for People and Planet. Nature 495:305–307.

900   Hoeting, J.A., D. Madigan, A.E. Raftery, and C.T. Volinsky, 1999. Bayesian Model Averaging:
901   A Tutorial. Statistical Science. doi:10.1214/ss/1009212519.

902   Hong, Y., D. Gochis, J. Cheng, K. Hsu, S. Sorooshian, Y. Hong, D. Gochis, J. Cheng, K. Hsu,
903   and S. Sorooshian, 2007. Evaluation of PERSIANN-CCS Rainfall Measurement Using the
904   NAME Event Rain Gauge Network. Journal of Hydrometeorology 8:469–482.

905   Hopson, T.M., 2014. Assessing the Ensemble Spread-Error Relationship. Monthly Weather
906   Review 142:1125–1142.

907   Hopson, T.M. and P.J. Webster, 2010. A 1-10-Day Ensemble Forecasting Scheme for the Major
908   River Basins of Bangladesh: Forecasting Severe Floods of 2003-07. Journal of
909   Hydrometeorology 11:618–641.

910   Huffman, G.J., D.T. Bolvin, E.J. Nelkin, D.B. Wolff, R.F. Adler, G. Gu, Y. Hong, K.P.
911   Bowman, E.F. Stocker, G.J. Huffman, D.T. Bolvin, E.J. Nelkin, D.B. Wolff, R.F. Adler, G.
912   Gu, Y. Hong, K.P. Bowman, and E.F. Stocker, 2007. The TRMM Multisatellite
913   Precipitation Analysis (TMPA): Quasi-Global, Multiyear, Combined-Sensor Precipitation
914   Estimates at Fine Scales. Journal of Hydrometeorology 8:38–55.

915   Immerzeel, W.W. and P. Droogers, 2008. Calibration of a Distributed Hydrological Model Based
916   on Satellite Evapotranspiration. Journal of Hydrology. doi:10.1016/j.jhydrol.2007.11.017.

917   Jiang, C. and Y. Ryu, 2016. Multi-Scale Evaluation of Global Gross Primary Productivity and
918   Evapotranspiration Products Derived from Breathing Earth System Simulator (BESS).
919   Remote Sensing of Environment 186:528–547.

920   Johnson, S.J., T.N. Stockdale, L. Ferranti, M.A. Balmaseda, F. Molteni, L. Magnusson, S.
921   Tietsche, D. Decremer, A. Weisheimer, G. Balsamo, S.P.E. Keeley, K. Mogensen, H. Zuo,
922   and B.M. Monge-Sanz, 2019. SEAS5: The New ECMWF Seasonal Forecast System.
923   Geoscientific Model Development. doi:10.5194/gmd-12-1087-2019.

924   Joyce, R.J., J.E. Janowiak, P.A. Arkin, P. Xie, R.J. Joyce, J.E. Janowiak, P.A. Arkin, and P. Xie,
925   2004. CMORPH: A Method That Produces Global Precipitation Estimates from Passive
926   Microwave and Infrared Data at High Spatial and Temporal Resolution. Journal of
927   Hydrometeorology 5:487–503.

928   Kirtman, B.P., D. Min, J.M. Infanti, J.L. Kinter, D.A. Paolino, Q. Zhang, H. Van Den Dool, S.
929   Saha, M.P. Mendez, E. Becker, P. Peng, P. Tripp, J. Huang, D.G. Dewitt, M.K. Tippett,
930   A.G. Barnston, S. Li, A. Rosati, S.D. Schubert, M. Rienecker, M. Suarez, Z.E. Li, J.
931   Marshak, Y.K. Lim, J. Tribbia, K. Pegion, W.J. Merryfield, B. Denis, and E.F. Wood, 2014.
932   The North American Multimodel Ensemble: Phase-1 Seasonal-to-Interannual Prediction;
933   Phase-2 toward Developing Intraseasonal Prediction. Bulletin of the American
934   Meteorological Society. doi:10.1175/BAMS-D-12-00050.1.

935   Knievel, J.C., Y. Liu, T.M. Hopson, J.S. Shaw, S.F. Halvorson, H.H. Fisher, G. Roux, R.S. Sheu,
936   L. Pan, W. Wu, J.P. Hacker, E. Vernon, F.W. Gallagher, and J.C. Pace, 2017. Mesoscale
937   Ensemble Weather Prediction at U.S. Army Dugway Proving Ground, Utah. Weather and
938   Forecasting 32:2195–2216.

939   Koenker, R. and G. Bassett, 1978a. Regression Quantiles. Econometrica. doi:10.2307/1913643.

940   Koenker, R. and G. Bassett, 1978b. Regression Quantiles. Econometrica 46:33.

941   Koppa, A. and M. Gebremichael, 2017. A Framework for Validation of Remotely Sensed
942   Precipitation and Evapotranspiration Based on the Budyko Hypothesis. Water Resources
943   Research 53. doi:10.1002/2017WR020593.

944   Koppa, A. and M. Gebremichael, 2020. Improving the Applicability of Hydrologic Models for

945   Food–Energy–Water Nexus Studies Using Remote Sensing Data. Remote Sensing 12:599.

946   Koppa, A., M. Gebremichael, and W.W.G. Yeh, 2019. Multivariate Calibration of Large Scale
947   Hydrologic Models: The Necessity and Value of a Pareto Optimal Approach. Advances in
948   Water Resources 130:129–146.

949   Koppa, A., M. Gebremichael, R.C. Zambon, W.W. -G. Yeh, and T.M. Hopson, 2019. Seasonal
950   Hydropower Planning for Data-Scarce Regions Using Multimodel Ensemble Forecasts,
951   Remote Sensing Data, and Stochastic Programming. Water Resources Research.
952   doi:10.1029/2019WR025228.

953   Kumar, S. V., C.D. Peters-Lidard, Y. Tian, P.R. Houser, J. Geiger, S. Olden, L. Lighty, J.L.
954   Eastman, B. Doty, P. Dirmeyer, J. Adams, K. Mitchell, E.F. Wood, and J. Sheffield, 2006.
955   Land Information System: An Interoperable Framework for High Resolution Land Surface
956   Modeling. Environmental Modelling and Software. doi:10.1016/j.envsoft.2005.07.004.

957   Leaflet, 2016. Leaflet - a JavaScript Library for Interactive Maps. Leaflet.Com.

958   Lettenmaier, D.P., D. Alsdorf, J. Dozier, G.J. Huffman, M. Pan, and E.F. Wood, 2015. Inroads of
959   Remote Sensing into Hydrologic Science during the WRR Era. Water Resources Research
960   51:7309–7342.

961   Li, W., Q. Duan, C. Miao, A. Ye, W. Gong, and Z. Di, 2017. A Review on Statistical
962   Postprocessing Methods for Hydrometeorological Ensemble Forecasting. Wiley
963   Interdisciplinary Reviews: Water 4:e1246.

964   Li, D., M. Pan, Z. Cong, L. Zhang, and E. Wood, 2013. Vegetation Control on Water and Energy
965   Balance within the Budyko Framework. Water Resources Research 49:969–976.

966   López, P.L., E.H. Sutanudjaja, J. Schellekens, G. Sterk, and M.F.P. Bierkens, 2017. Calibration
967   of a Large-Scale Hydrological Model Using Satellite-Based Soil Moisture and
968   Evapotranspiration Products. Hydrology and Earth System Sciences. doi:10.5194/hess-21-
969   3125-2017.

970   Martens, B., D.G. Miralles, H. Lievens, R. Van Der Schalie, R.A.M. De Jeu, D. Fernández-
971   Prieto, H.E. Beck, W.A. Dorigo, and N.E.C. Verhoest, 2017. GLEAM v3: Satellite-Based
972   Land Evaporation and Root-Zone Soil Moisture. Geoscientific Model Development.

973   doi:10.5194/gmd-10-1903-2017.

974   Mazrooei, A. and A. Sankarasubramanian, 2019. Improving Monthly Streamflow Forecasts
975   through Assimilation of Observed Streamflow for Rainfall-Dominated Basins across the
976   CONUS. Journal of Hydrology 575:704–715.

977   Merryfield, W.J., W.S. Lee, G.J. Boer, V. V. Kharin, J.F. Scinocca, G.M. Flato, R.S.
978   Ajayamohan, J.C. Fyfe, Y. Tang, and S. Polavarapu, 2013. The Canadian Seasonal to
979   Interannual Prediction System. Part I: Models and Initialization. Monthly Weather Review.
980   doi:10.1175/MWR-D-12-00216.1.

981   Mianabadi, A., K. Davary, M. Pourreza-Bilondi, and A.M.J. Coenders-Gerrits, 2020. Budyko
982   Framework; towards Non-Steady State Conditions. Journal of Hydrology.
983   doi:10.1016/j.jhydrol.2020.125089.

984   Mu, Q., M. Zhao, and S.W. Running, 2011. Improvements to a MODIS Global Terrestrial
985   Evapotranspiration Algorithm. Remote Sensing of Environment 115:1781–1800.

986   Ning, T., Z. Li, Q. Feng, W. Liu, and Z. Li, 2018. Comparison of the Effectiveness of Four
987   Budyko-Based Methods in Attributing Long-Term Changes in Actual Evapotranspiration.
988   Scientific Reports. doi:10.1038/s41598-018-31036-x.

989   Niu, G.Y., Z.L. Yang, K.E. Mitchell, F. Chen, M.B. Ek, M. Barlage, A. Kumar, K. Manning, D.
990   Niyogi, E. Rosero, M. Tewari, and Y. Xia, 2011. The Community Noah Land Surface
991   Model with Multiparameterization Options (Noah-MP): 1. Model Description and
992   Evaluation with Local-Scale Measurements. Journal of Geophysical Research Atmospheres.
993   doi:10.1029/2010JD015139.

994   Raftery, A.E., T. Gneiting, F. Balabdaoui, and M. Polakowski, 2005. Using Bayesian Model
995   Averaging to Calibrate Forecast Ensembles. Monthly Weather Review.
996   doi:10.1175/MWR2906.1.

997   Rakovec, O., R. Kumar, S. Attinger, and L. Samaniego, 2016. Improving the Realism of
998   Hydrologic Model Functioning through Multivariate Parameter Estimation. Water
999   Resources Research 52:7779–7792.

1000   Sachs, J.D., 2012. From Millennium Development Goals to Sustainable Development Goals. The

Lancet 379:2206–2211.

Séguin, S., C. Audet, and P. Côté, 2017. Scenario-Tree Modeling for Stochastic Short-Term Hydropower Operations Planning. Journal of Water Resources Planning and Management 143:04017073.

Senay, G.B., M.E. Budde, and J.P. Verdin, 2011. Enhancing the Simplified Surface Energy Balance (SSEB) Approach for Estimating Landscape ET: Validation with the METRIC Model. Agricultural Water Management 98:606–618.

Sheffield, J., E.F. Wood, M. Pan, H. Beck, G. Coccia, A. Serrat-Capdevila, and K. Verbist, 2018. Satellite Remote Sensing for Water Resources Management: Potential for Supporting Sustainable Development in Data-Poor Regions. Water Resources Research 54:9724–9758.

Sloughter, J.M.L., A.E. Raftery, T. Gneiting, and C. Fraley, 2007. Probabilistic Quantitative Precipitation Forecasting Using Bayesian Model Averaging. Monthly Weather Review. doi:10.1175/MWR3441.1.

Snow, A.D., S.D. Christensen, N.R. Swain, E.J. Nelson, D.P. Ames, N.L. Jones, D. Ding, N.S. Noman, C.H. David, F. Pappenberger, and E. Zsoter, 2016. A High-Resolution National-Scale Hydrologic Forecast System from a Global Ensemble Land Surface Model. Journal of the American Water Resources Association. doi:10.1111/1752-1688.12434.

Sorooshian, S., K.-L. Hsu, X. Gao, H. V. Gupta, B. Imam, D. Braithwaite, S. Sorooshian, K.-L. Hsu, X. Gao, H. V. Gupta, B. Imam, and D. Braithwaite, 2000. Evaluation of PERSIANN System Satellite–Based Estimates of Tropical Rainfall. Bulletin of the American Meteorological Society 81:2035–2046.

Sridharan, V., O. Broad, A. Shivakumar, M. Howells, B. Boehlert, D.G. Groves, H.H. Rogner, C. Taliotis, J.E. Neumann, K.M. Strzepek, R. Lempert, B. Joyce, A. Huber-Lee, and R. Cervigni, 2019. Resilience of the Eastern African Electricity Sector to Climate Driven Changes in Hydropower Generation. Nature Communications 10:1–9.

Taylor, K.E., 2001. Summarizing Multiple Aspects of Model Performance in a Single Diagram. Journal of Geophysical Research Atmospheres. doi:10.1029/2000JD900719.

Tramontana, G., M. Jung, C.R. Schwalm, K. Ichii, G. Camps-Valls, B. Ráduly, M. Reichstein,

1029   M.A. Arain, A. Cescatti, G. Kiely, L. Merbold, P. Serrano-Ortiz, S. Sickert, S. Wolf, and D.
1030   Papale, 2016. Predicting Carbon Dioxide and Energy Fluxes across Global FLUXNET Sites
1031   with Regression Algorithms. Biogeosciences 13:4291–4313.

1032 Unger, D.A., H. van den Dool, E. O'Lenic, and D. Collins, 2009. Ensemble Regression. Monthly
1033   Weather Review. doi:10.1175/2008MWR2605.1.

1034 Vrugt, J.A., C.J.F. ter Braak, M.P. Clark, J.M. Hyman, and B.A. Robinson, 2008. Treatment of
1035   Input Uncertainty in Hydrologic Modeling: Doing Hydrology Backward with Markov
1036   Chain Monte Carlo Simulation. Water Resources Research. doi:10.1029/2007wr006720.

1037 Vrugt, J.A., C.J.F. Ter Braak, C.G.H. Diks, B.A. Robinson, J.M. Hyman, and D. Higdon, 2009.
1038   Accelerating Markov Chain Monte Carlo Simulation by Differential Evolution with Self-
1039   Adaptive Randomized Subspace Sampling. International Journal of Nonlinear Sciences and
1040   Numerical Simulation. doi:10.1515/IJNSNS.2009.10.3.273.

1041 Wang, F., L. Wang, H. Zhou, O.C. Saavedra Valeriano, T. Koike, and W. Li, 2012. Ensemble
1042   Hydrological Prediction-Based Real-Time Optimization of a Multiobjective Reservoir
1043   during Flood Season in a Semiarid Basin with Global Numerical Weather Predictions.
1044   Water Resources Research 48. doi:10.1029/2011WR011366.

1045 Westphal, K.S., R.M. Vogel, P. Kirshen, and S.C. Chapra, 2003. Decision Support System for
1046   Adaptive Water Supply Management. Journal of Water Resources Planning and
1047   Management 129:165–177.

1048 Wielicki, B.A., B.R. Barkstrom, E.F. Harrison, R.B. Lee, G. Louis Smith, J.E. Cooper, B.A.
1049   Wielicki, B.R. Barkstrom, E.F. Harrison, R.B.L. III, G.L. Smith, and J.E. Cooper, 1996.
1050   Clouds and the Earth's Radiant Energy System (CERES): An Earth Observing System
1051   Experiment. Bulletin of the American Meteorological Society 77:853–868.

1052 Xu, X., W. Liu, B.R. Scanlon, L. Zhang, and M. Pan, 2013. Local and Global Factors
1053   Controlling Water-Energy Balances within the Budyko Framework. Geophysical Research
1054   Letters 40:6123–6129.

1055 Yamazaki, D., D. Ikeshima, R. Tawatari, T. Yamaguchi, F. O'Loughlin, J.C. Neal, C.C.
1056   Sampson, S. Kanae, and P.D. Bates, 2017. A High-Accuracy Map of Global Terrain

1057   Elevations. Geophysical Research Letters 44:5844–5853.

1058 Yeh, W.W.-G., 1985. Reservoir Management and Operations Models: A State-of-the-Art

1059   Review. Water Resources Research 21:1797–1818.

1060 Zhang, K., J.S. Kimball, R.R. Nemani, and S.W. Running, 2010. A Continuous Satellite-Derived

1061   Global Record of Land Surface Evapotranspiration from 1983 to 2006. Water Resources

1062   Research 46. doi:10.1029/2009WR008800.

1063 Zhang, Y., J.L. Peña-Arancibia, T.R. McVicar, F.H.S. Chiew, J. Vaze, C. Liu, X. Lu, H. Zheng,

1064   Y. Wang, Y.Y. Liu, D.G. Miralles, and M. Pan, 2016. Multi-Decadal Trends in Global

1065   Terrestrial Evapotranspiration and Its Components. Scientific Reports 6:19124.

1066 Zhou, G., X. Wei, X. Chen, P. Zhou, X. Liu, Y. Xiao, G. Sun, D.F. Scott, S. Zhou, L. Han, and

1067   Y. Su, 2015. Global Pattern for the Effect of Climate and Land Cover on Water Yield.

1068   Nature Communications. doi:10.1038/ncomms6918.

1069 Zink, M., J. Mai, M. Cuntz, and L. Samaniego, 2018. Conditioning a Hydrologic Model Using

1070   Patterns of Remotely Sensed Land Surface Temperature. Water Resources Research.

1071   doi:10.1002/2017WR021346.

1072

1073

1074

1075

1076

1077

1078

1079

1080

1081 **List of Tables**

1082   **Table 1.** List of satellite-based precipitation, terrestrial evaporation, and net radiation datasets

1083   implement in the decision support system.

Data source	Spatial resolution (degree)	Temporal resolution (years)	Spatial Coverage (degree)	Reference
Precipitation				
CHIRPSv2.0	0.05	1981–2019	50N-50S	(Funk, Peterson, *et al.*, 2015)
CMORPHv0.x.RAW	0.25	2002–2017	60N-60S	(Joyce *et al.*, 2004)
PERSIANN	0.25	2000–2019	60N-60S	(Sorooshian *et al.*, 2000)
PERSIANN.CCS	0.04	2003–2019	60N-60S	(Hong *et al.*, 2007)
PERSIANN.CDR	0.25	1983–2016	60N-60S	(Ashouri *et al.*, 2015)
TRMM.3B42RT	0.25	2000–2019	50N-50S	(Huffman *et al.*, 2007)
TRMM.3B43	0.25	2000–2019	50N-50S	(Huffman *et al.*, 2007)
Terrestrial Evaporation				
AVHRR.NTSG	0.08	1983–2013	Global	(Zhang *et al.*, 2010)
SSEBOpv4.0	0.01	2003–2019	Global	(Senay *et al.*, 2011)
MOD16A3	0.05	2000–2014	Global	(Mu *et al.*, 2011)
GLEAMv3.3a	0.25	1980–2018	Global	(Martens *et al.*, 2017)
CSIRO-PMLv2.0	0.5	1981–2012	Global	(Zhang *et al.*, 2016)
BESS	0.5	2000–2015	Global	(Jiang and Ryu, 2016)
FluxCom.RS	0.5	2001–2015	Global	(Tramontana *et al.*, 2016)
Net Radiation				

CERESv4.0	1.0	2000–2018	Global	(Wielicki *et al.*, 1996)
Precipitation Forecasts				
China Meteorological Administration (CMA)	0.5	2006-Present	Global	-
Center for Weather Forecast and Climate Studies, Brazil (CPTEC)	0.94	2006-Present	Global	-
European Center for Medium Range Weather Forecast (ECMWF)	0.75	2006-Present	Global	-
MeteoFrance	0.3	2006-Present	Global	-
UKMet	0.2	2006-Present	Global	-
Japanese Meteorological Agency (JMA)	1.25	2006-Present	Global	-
National Centers for Environmental Prediction	1.0	2006-Present	Global	-

1084

1085

1086

1087

1088 **Table 2**. Details of the five hydropower reservoirs in the Omo-Gibe River basin

Reservoir Name	Start of Operation	Hydropower Capacity	Maximum Storage
Gilgel Gibe I	2004	210 MW	840 Mm^3
Gilgel Gibe II	2010	420 MW	0.15 Mm^3 (Run-of-river)
Gilgel Gibe III	2015	1870 MW	13700 Mm^3

| Koysha Dam | Planned | 2160 MW | - |
| Halele Wera | 2014 | 424 MW | - |

1089

1090

1091

1092

1093

Table 3. Noah-MP model physics options

Model Physics	Selected Physics Option
Vegetation model	Use table Leaf Area Index (4)
Canopy stomatal resistance	Ball-Berry (1) [*Ball et al.*, 1987]
Soil moisture factor for stomatal resistance	Original Noah (1) [*Chen et al.*, 1997]
Runoff and groundwater	TOPMODEL with groundwater (1) [*Niu et al.*, 2007]
Surface layer drag coefficient	Original Noah (2) [*Chen et al.*, 1997]
Frozen soil permeability	Linear effects, more permeable (1) [*Niu and Yang*, 2006]
Radiation transfer	Modified two-stream (1) [*Yang and Friedl*, 2003]
Snow surface albedo	CLASS (2) [*Verseghy et al.*, 1991]
Rainfall and snowfall Partitioning	Jordan Scheme(1) [*Jordan*, 1991]
Lower boundary of soil temperature	Original Noah (2) [*Chen et al.*, 1997]
Snow and soil temperature time scheme	Semi-implicit (1)

| | Super-cooled liquid water | No iteration [*Niu and Yang*, 2006] (1) |

1094   ^a The number in the brackets represents the internal Noah-MP model code for the selected

1095   physics option

1096

1097   **Table 4.** Details of Noah-MP parameters used for calibration

Parameter	Description	Sensitive Variable	Total Parameters	Units	Minimum	Maximum
REFDK	Surface runoff parameter	SF	1	m/s	1.4e-06	6.5e-06
REFKDT	Surface runoff parameter	SF	1	No Units	1.0	5.0
BB1 - BB12	Exponent in the Brooks Corey Equation	SF, ET	12	No Units	0.5	12.0
MAXSMC1 - MAXSMC12	Soil porosity	SF, ET	12	No units	0.1	0.7
SATDK1 - SATDK12	Saturated hydraulic conductivity	SF, ET	12	m/s	2.0e-06	7.0e-02

1098   ^a Soil texture classes for BB, MAXSMC and SATDK (from 1 - 12): Sand, Loamy

1099   sand, Sandy loam, Silt loam, Silt, Loam, Sandy clay loam, Silt clay loam, Clay loam, Sandy clay,

1100   Silty clay and Clay.

1101

1102   **Table 5.** MT-DREAM (ZS) and AMALGAM configuration

DREAM Option	Specified Option
Number of generations	600
Number of Markov chains	3
Number of forward model parameters	38
Number of crossover values	3
Number of Multi-tries	4
Number of chain pairs proposal	1
Prior Distribution	Uniform
Likelihood function	Laplacian likelihood

[a] Note: All other MT-DREAM (ZS) parameters are set to default values

Table 6. Comparison of Actual and Optimized Power Production for the Planning Horizon (Feb 2005 to Sep 2005)

Scenario	Gibe I	Gibe III
	Power Produced (million MWh)	Power Produced (million MWh)
Actual	0.53	-
DET	0.68	1.96
SPWR-D	0.71	1.96
SPWR-S	0.76	2.10
SEASN	0.54	1.84

1112

1113

1114

1115

1116

1117

1118 Figure Captions

1119 **Figure 1.** Block diagram of the hydropower Decision Support System (DSS).

1120 **Figure 2.** Location Schematic of the QR post-processing procedure.

1121 **Figure 3.** Processing steps for the rainfall displays of our interactive visualization module.

1122 **Figure 4.** Location map of the Omo-Gibe river basin in Ethiopia, and its watershed map showing
1123 locations of the five hydropower reservoirs. Red dots represent the dams modelled in this study.
1124 The green line represents a tunnel which connects Gibe I and Gibe II reservoirs.

1125 **Figure 5.** Heat map of the root mean square error (RMSE) of the combination of precipitation (P),
1126 on the x-axis, and terrestrial evaporation (ET) datasets, on the y-axis, for the Omo-Gibe river basin.
1127 The values are scaled between 0 and 1, with 0 representing the least performing combination and
1128 1 representing the best performing combination. The red star represents the best combination of P
1129 and ET dataset for the Omo-Gibe river basin.

1130 **Figure 6.** Heat Composites of June–September average precipitation anomalies corresponding to
1131 each phase of the MJO. Periods with no MJO activity are not shown.

1132 **Figure 7.** Composites of June-September standardized precipitation anomaly over Ethiopia
1133 during the El Nino phase of ENSO, with significant values shown with stippling, such as the
1134 north-northwest region of the country. Broken down by month (not shown), the July-August
1135 (rainfall peak season) and September (late season) show similar results, but there is no coherent
1136 pattern during June (early season).

1137 **Figure 8.** Visualization Module rainfall estimates and forecasts are provided at two different basin-

1138 averaged spatial-scales over East Africa as provided by the EROS Data Center hydro 1K dataset

1139 (top two panels). Over Ethiopia, the lowest resolution basin-averaged rainfall was provided basin-

1140 averaged over the 13 major river catchments of Ethiopia (lower right), with a special high

1141 resolution provided in the Omo Gibe for upstream catchments areas above the major reservoirs

1142 and measurement sites (lower left).

1143 **Figure 9.** Taylor diagrams of precipitation (P) forecasts from the CanCM3, CanCM4, GEOS-5,

1144 Ensemble Bayesian Model Average (BMA), and Ensemble mean models derived for different lead

1145 times (1-4 months) and for the calibration (12 months of 2004) and validation (12 months of 2005)

1146 time periods. The CanCM3, CanCM4, and GEOS-5 values are calculated as the mean of the 10

1147 ensemble members from each of the models. "Ensemble BMA" and "Ensemble Mean" are the

1148 simple mean and the BMA of all the 30 ensemble members across all the three models.

1149 **Figure 10.** Calibrated forecast of Blue Nile summertime precipitation using a weighted average

1150 of ENSO plus the 8 NMME models. June 1st forecast of June – September rainfall. The year

1151 being forecast is left out when calculating forecast weights and regression coefficients. Red –

1152 CenTrends precipitation data, Blue – Optimized ensemble forecast for mean rainfall (R=0.59,

1153 p<0.001), Blue shading – 80% confidence interval of the forecast.

1154 **Figure 11.** Brier skill scores for NCEP CFSv2 NWP 5-day accumulated rainfall forecasts over

1155 the Omo-Gibe river basin (black line) as a function of lead-time (days), and a combined quantile

1156 regression model utilizing MJO phase and anomaly information along with CFSv2 (green line),

1157 showing the appreciable improvement in forecasting skill that comes with the inclusion of the

1158 MJO at all lead-times.

1159 **Figure 12.** Brier skill score for precipitation exceeding the catchment-specific 90th percentile of

1160 rain after bias correction, showing how the multi-model forecast is equal to or out-performs any

1161 individual model for all of the 12 primary Ethiopian river basins shown. The lower right plot

1162 displays the precipitation amount corresponding to the catchment-specific 90th percentile. +24 hr

1163 ensemble forecasts were used to create these plots.

1164 **Figure 13.** a) Time series comparison of terrestrial evaporation (ET) from ET-calibrated Noah-

1165 MP model (green) and EOS-based ET estimates (black) from SSEBOpv4.0 for the calibration (12

1166   months of 2004) and validation (12 months of 2005) time periods. The 5% and 95% quantiles are

1167   from the behavioral solutions of Bayesian calibration. The vertical demarcates the calibration and

1168   validation time periods. b) Reservoir inflow forecasts into Gibe I and Gibe III reservoirs for the 8-

1169   month planning horizon (February-September 2005) and three scenarios: deterministic (DET),

1170   climatological reservoir inflow (SEASN), and stochastic (SPWR-S represented by the box plots).

1171   Note: the results in (b) correspond to the first stage of each iteration of the deterministic and

1172   stochastic programming with recourse model.

1173   **Figure 14.** a) Optimal release decisions and b) power produced in the Gibe I and Gibe III reservoirs

1174   for the 8-month planning horizon (February-September 2005) and four scenario structures: DET,

1175   SPWR-D, SPWR-S and SEASN (climatological reservoir inflows). Note: the results correspond

1176   to the first stage of each iteration of the deterministic and stochastic programming with recourse

1177   model.

1178   **Figure 15.** GUI for the dissemination of catchment precipitation data to stake holders. Forecasts

1179   are available from the NMME seasonal models (monthly and 3-month averages), as well as from

1180   the TIGGE models (1-day and 5-day averages) going out 2 weeks. Recent satellite observations

1181   are also available at the same time scales. Precipitation data are displayed at two different

1182   resolutions which can be accessed by zooming in and out and for both a large East Africa domain,

1183   as well as a more focused Ethiopia domain that includes the Blue Nile and Omo-Gibe basins. For

1184   the Omo-Gibe basin, the data are available on catchments upstream of local gauging sites. In

1185   addition to the map display, users can assess the data in graphical form as well as for download as

1186   a text file.

jawr_12914_f1.tif

Step 1: Determine climatological quantiles
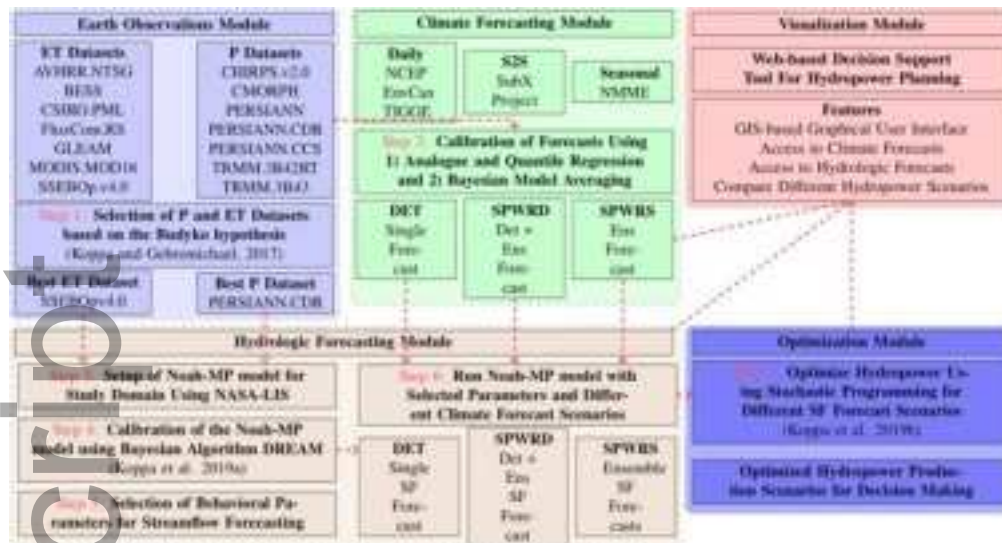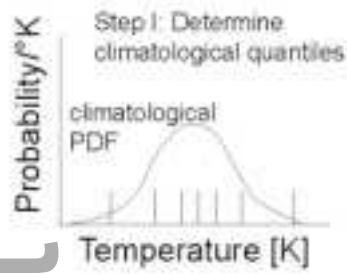
Step 2: For each quan, use forward step-wise cross-validation to select best regress set
Selection requires: a) min QR cost function.
b) binomial distrib at 95% confidence
If requirements not met, retain climatological "prior"

Regressor set
1. reforecast ens
2. ens mean
3. ens stdev
4. persistence
5. LR quantile
(not shown)
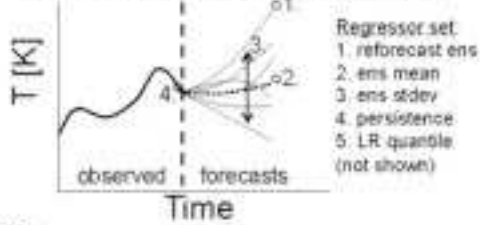
Step 3: segregate forecasts based on ens dispersion; refit models (Step 2) for each range
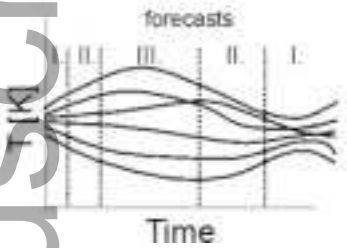
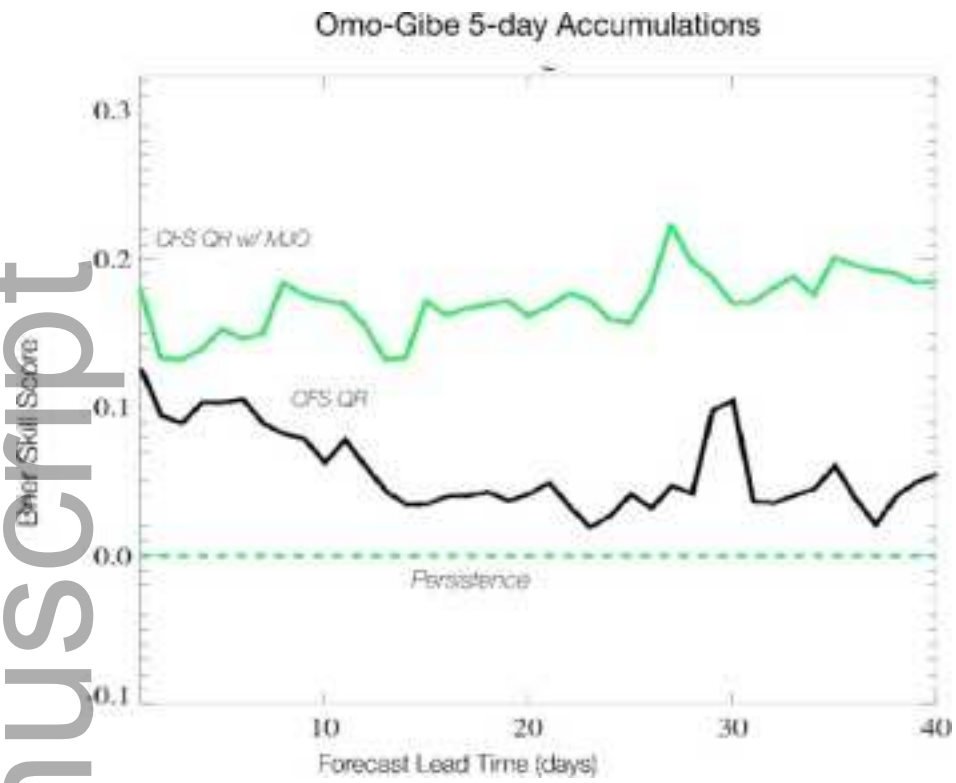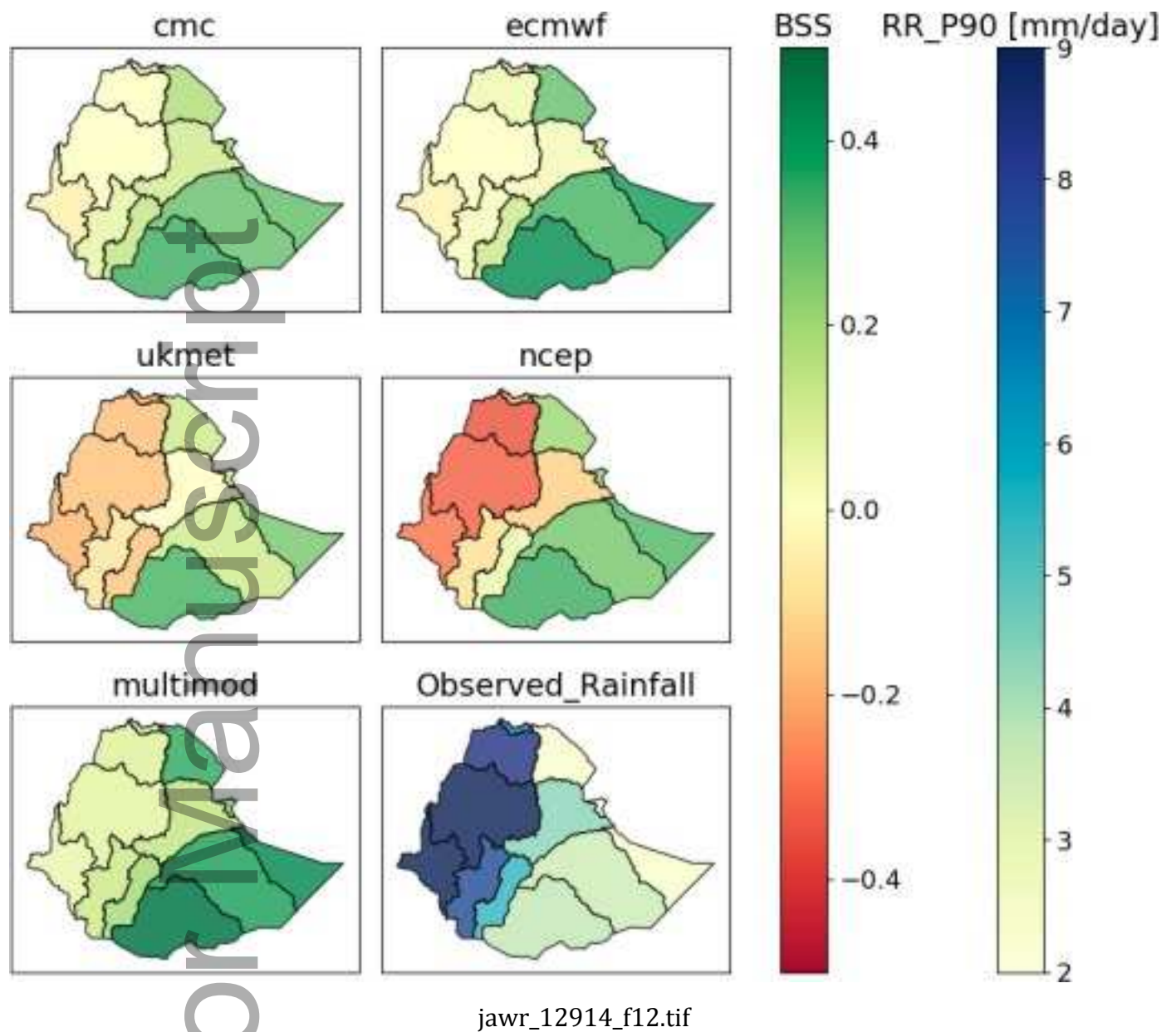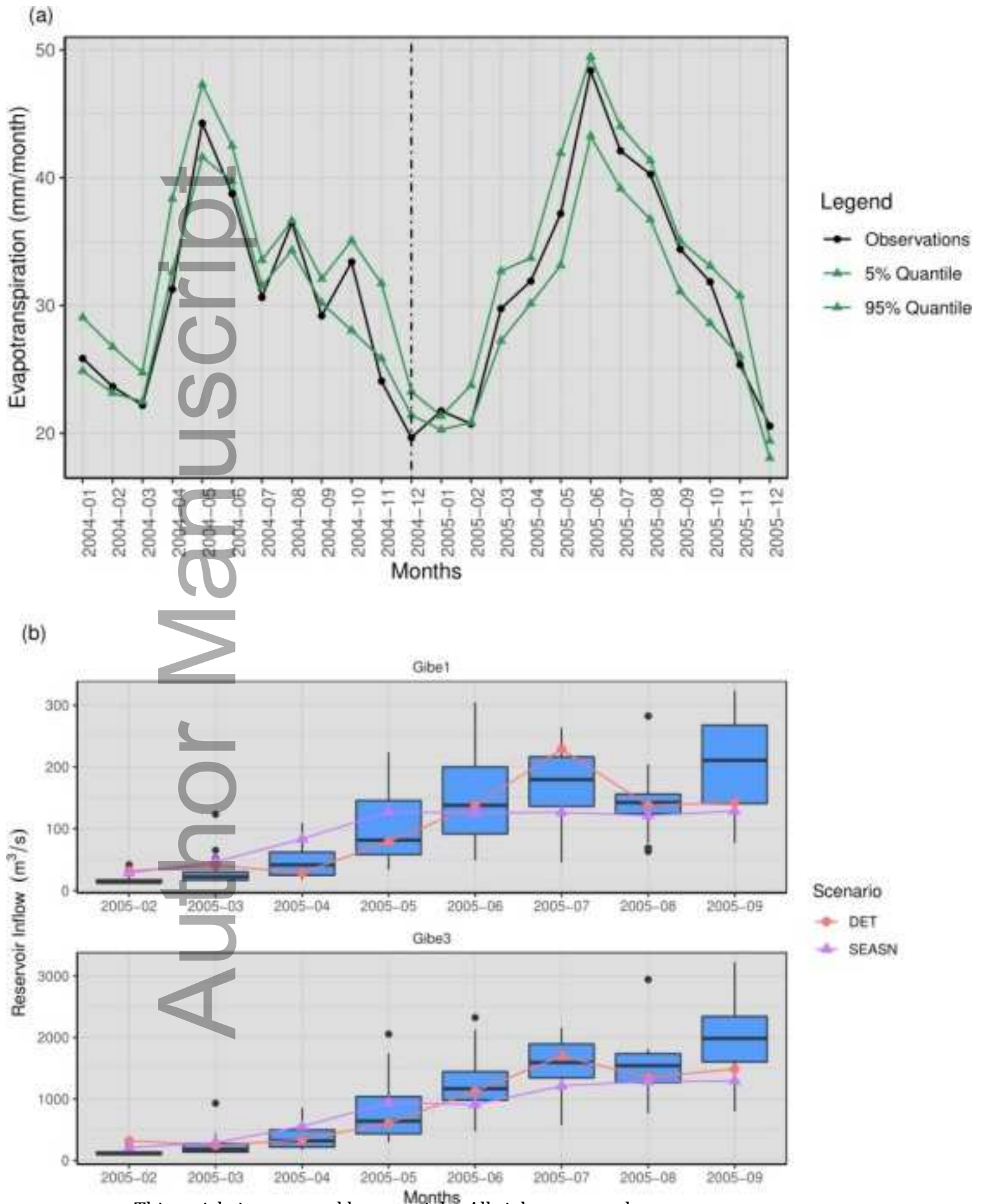Final result: "sharper" posterior PDF represented by interpolated quans
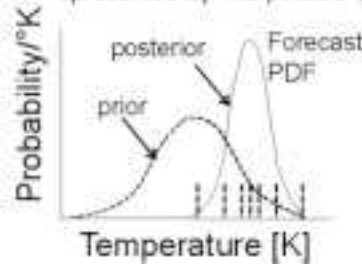
jawr_12914_f2.tif
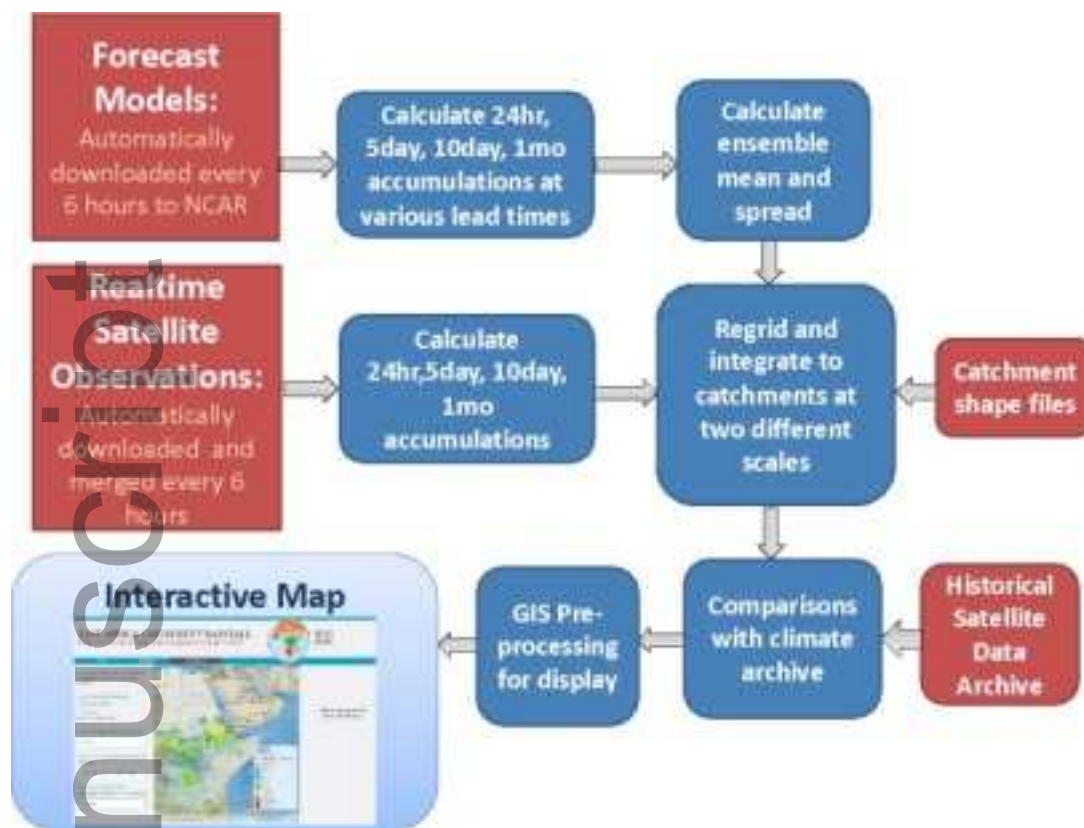
jawr_12914_f3.tif
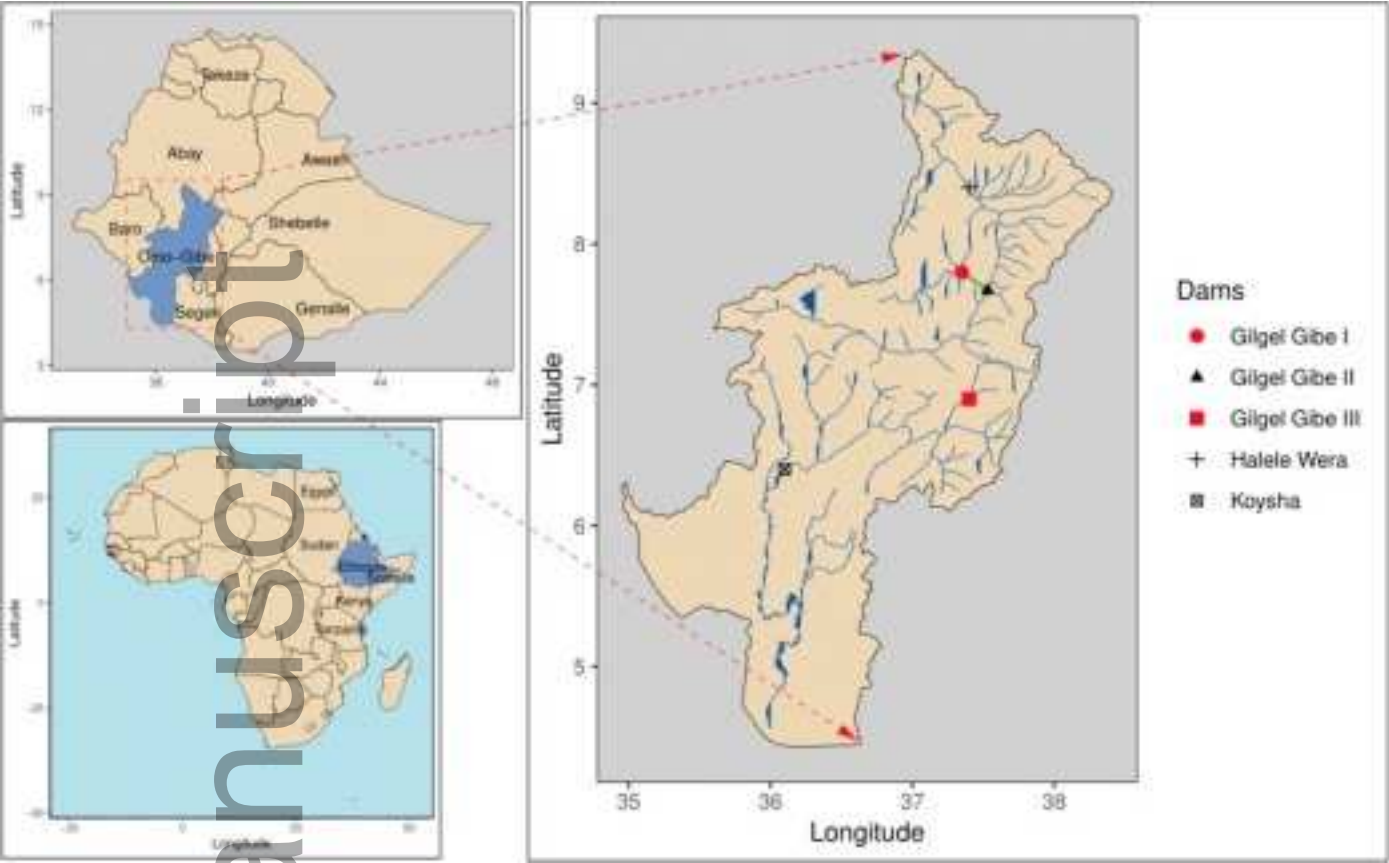
jawr_12914_f4.tif

jawr_12914_f5.tif

JJAS MJO RMM Phase Composites
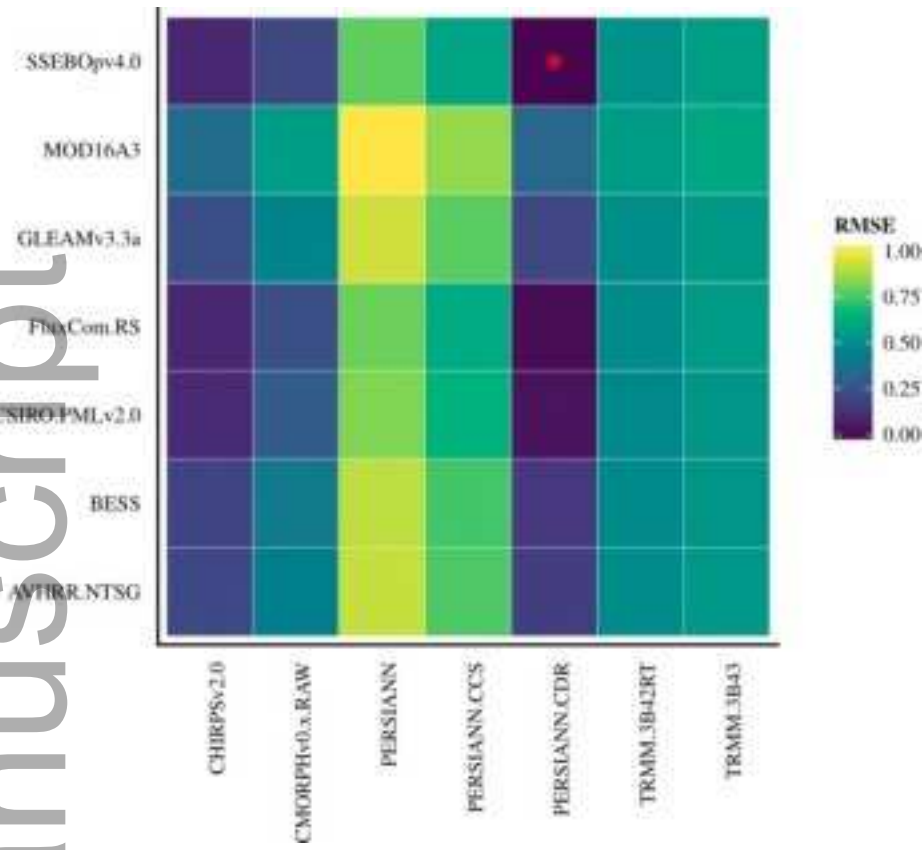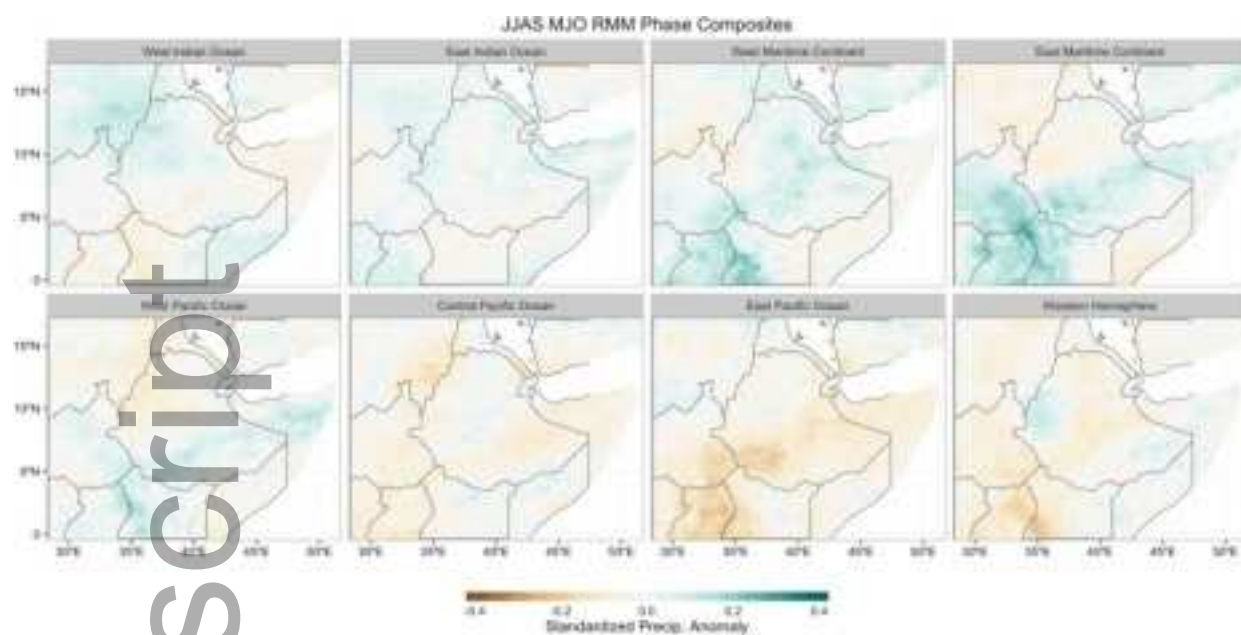
jawr_12914_f6.tif
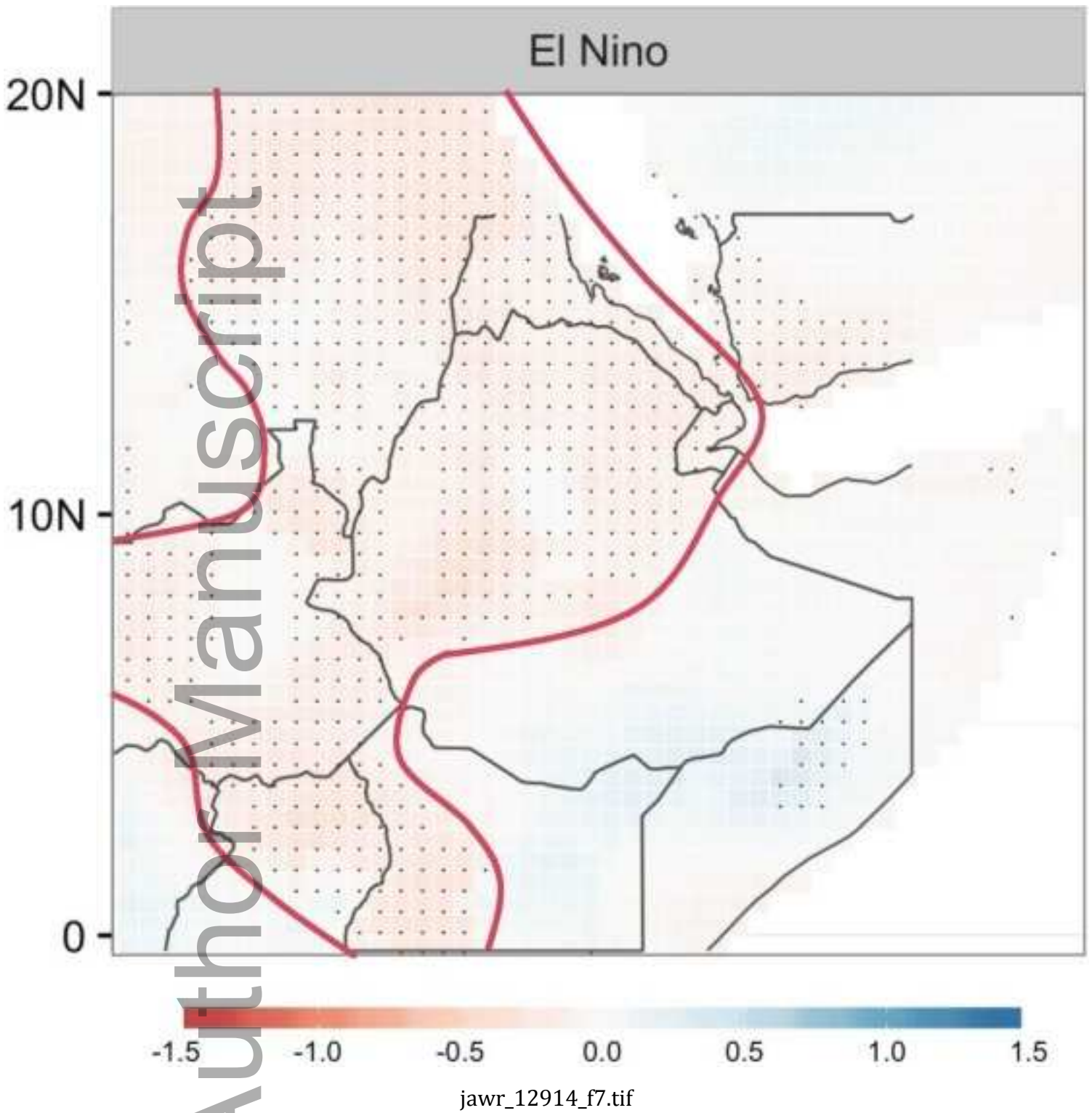
jawr_12914_f7.tif

Low resolutions catchments
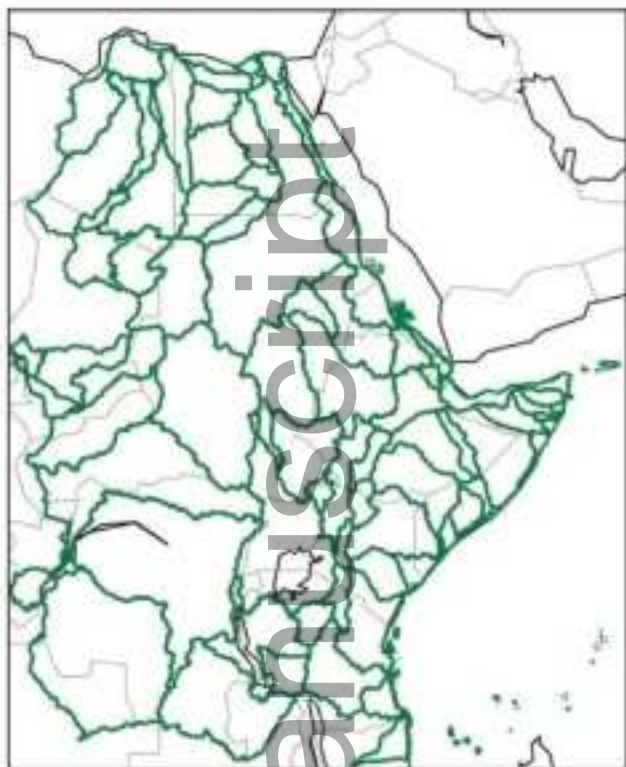
High resolutions catchments
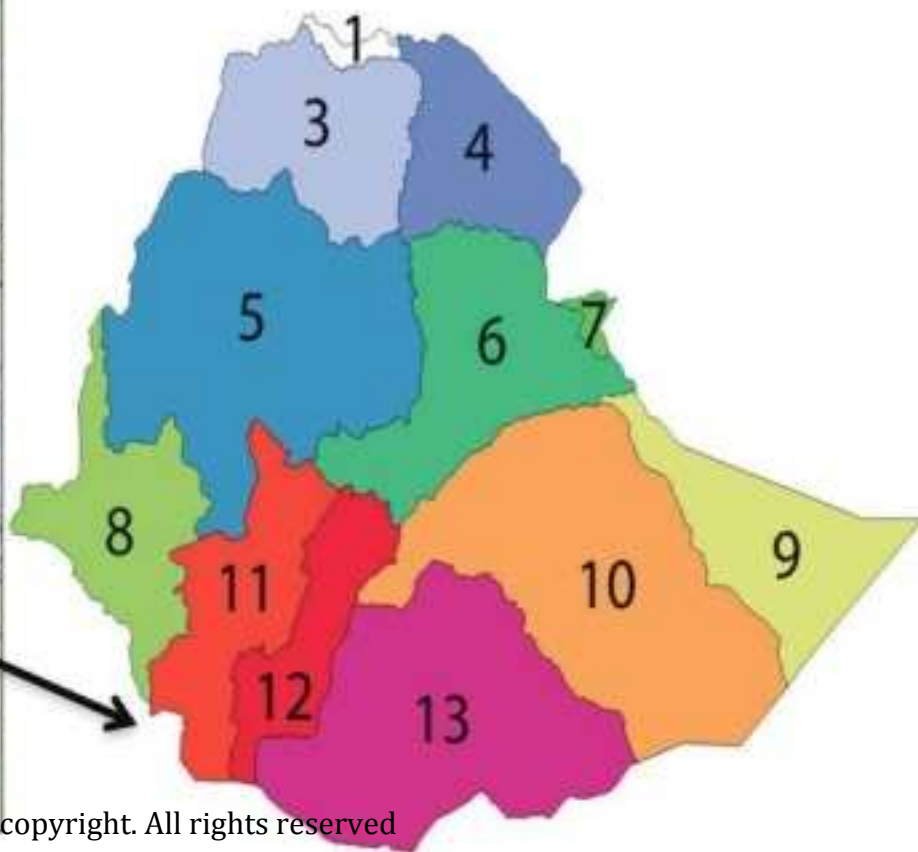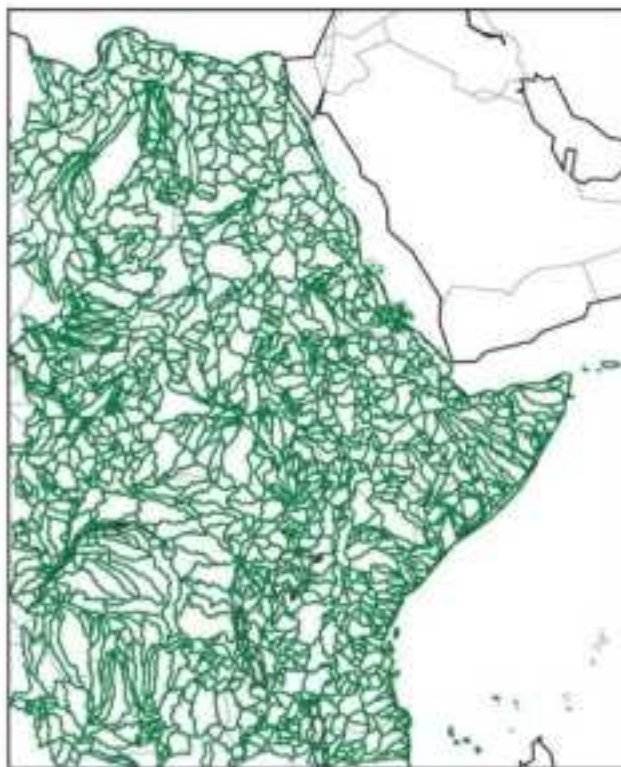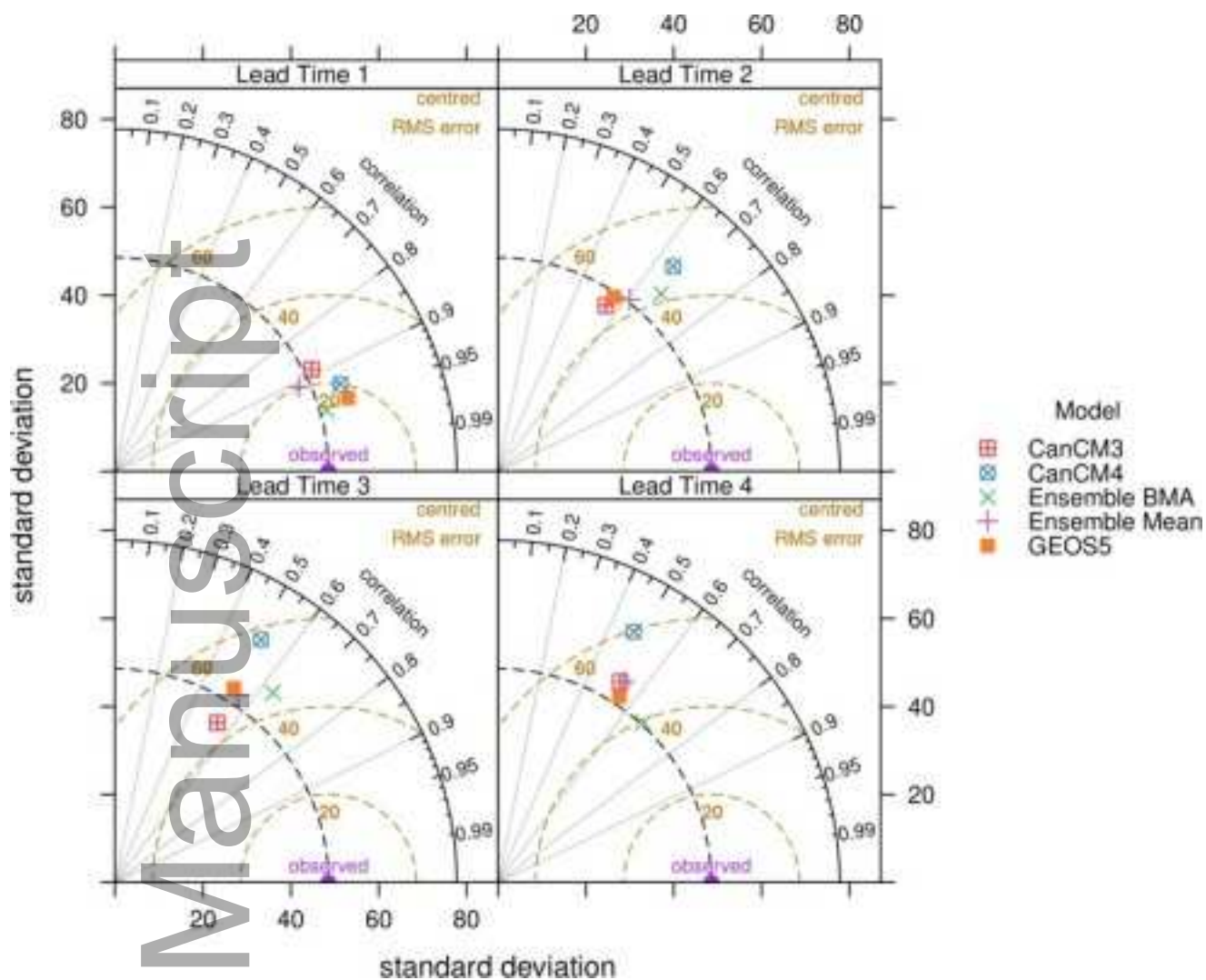
jawr_12914_f8.tif

jawr_12914_f9.tif

jawr_12914_f10.tif

Omo-Gibe 5-day Accumulations

jawr_12914_f11.tif

cmc ecmwf

ukmet ncep

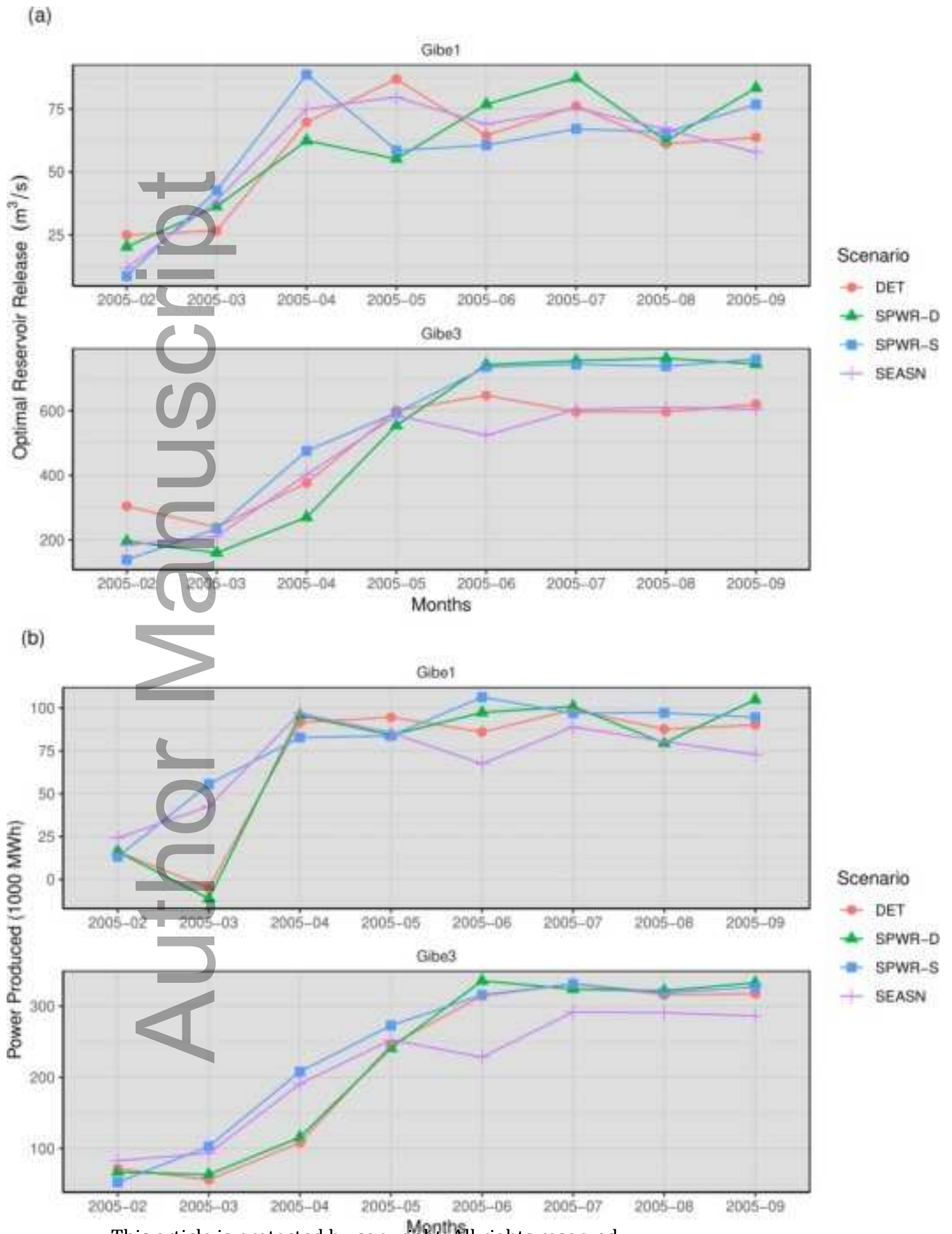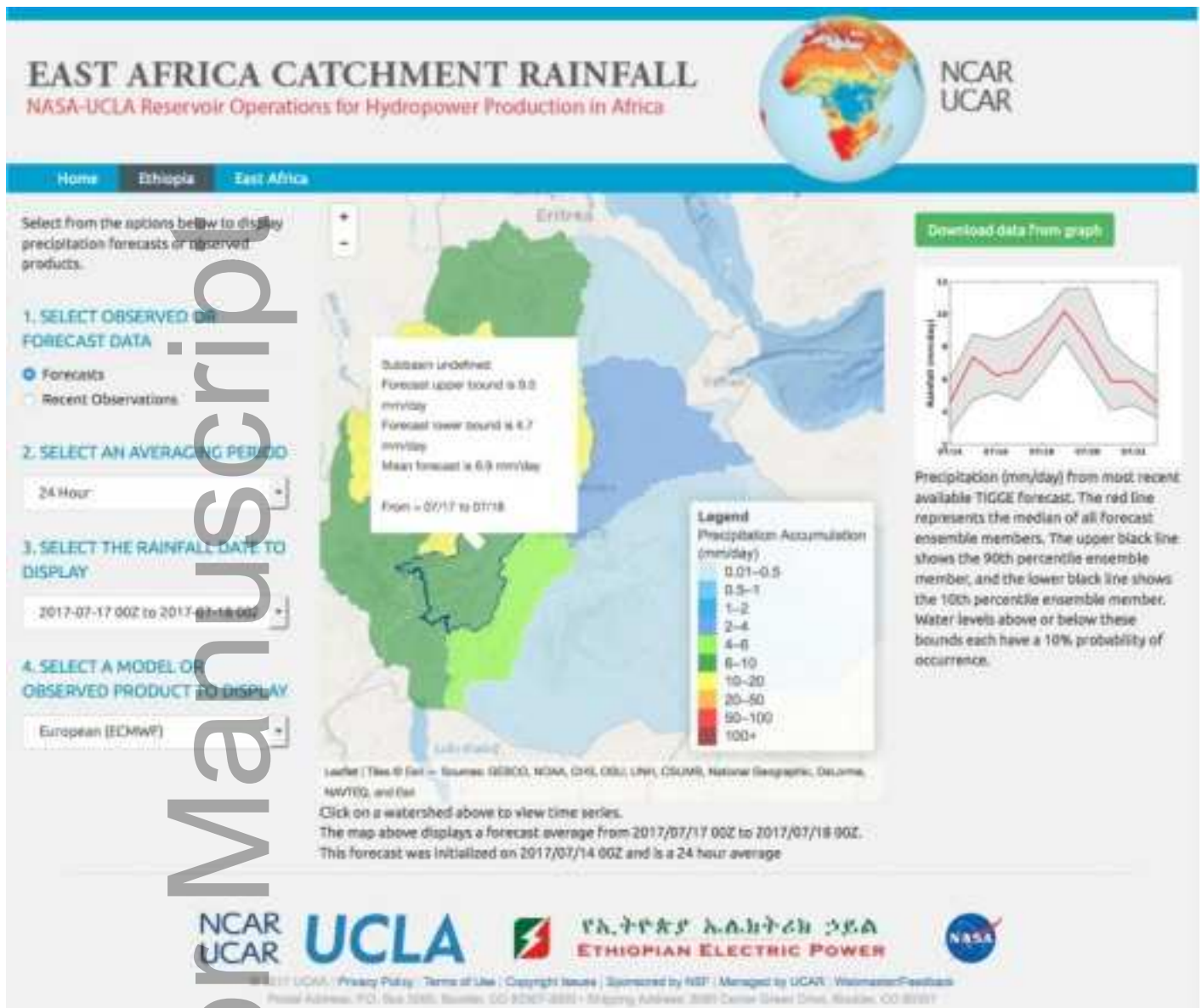multimod Observed_Rainfall

BSS RR_P90 [mm/day]

jawr_12914_f12.tif

jawr_12914_f13.tif

jawr_12914_f14.tif

jawr_12914_f15.tif